



Chem Soc Rev

Sensing and capture of toxic and hazardous chemical species in vapor phase by metal-organic frameworks

Journal:	<i>Chemical Society Reviews</i>
Manuscript ID	CS-REV-12-2017-000885.R1
Article Type:	Review Article
Date Submitted by the Author:	12-Feb-2018
Complete List of Authors:	Wang, Hao; Rutgers University, Chemistry and Chemical Biology Lustig, William; Rutgers University, Chemistry and Chemical Biology Li, Jing; Rutgers The State University of New Jersey

SCHOLARONE™
Manuscripts



Journal Name

ARTICLE

Sensing and Capture of Toxic and Hazardous Gases and Vapors by Metal-Organic Frameworks

Hao Wang,[†] William P. Lustig[†] and Jing Li^{*}Received 00th January 20xx,
Accepted 00th January 20xx

DOI: 10.1039/x0xx00000x

www.rsc.org/

Toxic and hazardous chemical species are ubiquitous, predominantly emitted by anthropogenic activities, and pose serious risks to human health and the environment. Thus, the sensing and subsequent capture of these chemicals, especially in the gas or vapor phase, are of extreme importance. To this end, metal-organic frameworks have attracted significant interest, as their high porosity and wide tunability make them ideal for both applications. These tailorable framework materials are particularly promising for the specific sensing and capture of targeted chemicals, as they can be designed to fit a diverse range of required conditions. This review will discuss the advantages of metal-organic frameworks in the sensing and capture of harmful gases and vapors, as well as principles and strategies guiding the design of these materials. Recent progress in the luminescent detection of aromatic and aliphatic volatile organic compounds, toxic gases, and chemical warfare agents will be summarized, and the adsorptive removal of fluorocarbons/chlorofluorocarbons, volatile radioactive species, toxic industrial gases and chemical warfare agents will be discussed.

1. Introduction

Metal-organic frameworks or MOFs, are coordination networks containing potential voids, following IUPAC recommendations.¹ Owing to their fascinating structural chemistry and enormous potential in industrial applications, MOFs have drawn tremendous attention over the past two decades from both scientific researchers and industrial engineers. As MOFs are built by coordinative bonds between metal nodes (metal ions or clusters) and organic linkers, a nearly infinite number of MOFs can be achieved by altering their connectivity or changing the identity of either metal or ligand. The unique features of MOFs include exceptionally high porosity (BET surface area up to 7000 m² g⁻¹, and pore volume up to 4.4 cm³ g⁻¹),² compositional and structural diversity, and highly tunable pore shape/size and surface functionality, to name a few.³ Fundamental studies with respect to the coordination, connectivity, and topology of MOFs have greatly enriched the knowledge and extended the horizon of chemists in the field, while the exploration of MOFs for industrial applications has continued to accelerate.^{4, 5} As a family of multifunctional materials, MOFs have been extensively studied for various potential applications including gas storage,⁶⁻⁹ molecular separations,¹⁰⁻¹⁴ catalysis,¹⁵⁻¹⁸ chemical sensing,¹⁹⁻²² proton conductivity,²³⁻²⁶ and many others.^{27, 28} In some of these areas MOFs have outperformed traditional or benchmark materials, or have shown potential value for commercialization. For example, a recently reported

microporous MOF is capable of separating propane and propylene through selective molecular exclusion which is not achievable by traditional zeolite materials.²⁹ More recently, the chemical company BASF developed a MOF-based natural gas storage system and have been testing it in demonstration vehicles, indicating that this technology is getting close to the market.³⁰ Additionally, TruPick, a post-harvest freshness management tool for fruits and vegetables built on MOF adsorbent, has already been used commercially in the United States. The technology uses MOFs for the storage and release of 1-methylcyclopropene (1-mcp), with the goal of prolonging the time over which fruits and vegetables can be safely stored.³⁰ There are a great many other examples wherein MOFs have shown enormous promise for implementation in real-world systems, particularly those associated with issues concerning energy and the environment. Among these is the sensing and capture of hazardous gases and vapors.

1.1. Hazardous gases and vapors, sources and importance of sensing and capture

Hazardous gases and vapors, including but not limited to toxic industrial gases (CO_x, NH₃, SO_x, NO_x, H₂S etc.), volatile organic compounds (VOCs, such as hydrocarbons, fluorocarbons, chlorofluorocarbons, etc.), volatile radioactive species, and chemical warfare agents, are a major threat to human health and the environment.³¹⁻³³ These hazardous gases and vapors are mainly released into the atmosphere from anthropogenic sources including power plants, factories, and household emissions, to name a few. For example, the sharply rising level of atmospheric carbon dioxide is predominantly attributed to the combustion of coal, oil, and natural gas which accounts for 80% of the CO₂ emission

Department of Chemistry and Chemical Biology, Rutgers University, Piscataway, NJ 08854, USA. E-mail: jingli@rutgers.edu

[†] These authors contributed equally to this work

worldwide.^{34, 35} In addition, the emission of volatile radioactive species such as iodine and organic iodides is primarily associated with the implementation of nuclear power.^{36, 37} Chemical warfare agents such as sarin and sulfur mustard have been frequently used in localized conflicts and terrorist attack.³⁸ Toxic industrial gases are ubiquitous in industrial processes, and chemical workers or related personnel are at risk of exposure in case of any accidental spillage or leakage; Chlorofluorocarbons, mostly emitted from the use of refrigerants, are responsible for the depletion of ozone layer.³⁹ In light of the impacts that hazardous gases and vapors have on human health and the environment, developing effective technologies for the sensing and capture of toxic chemicals and environmental pollutants are therefore of global importance and highly necessary. Advanced sensor materials will enable fast detection of the presence of toxic or hazardous species, and adsorbent materials that can effectively capture toxic and hazardous gases and vapors are vital for their removal and subsequent sequestration.

1.2. Luminescent MOFs (LMOFs) as chemosensors, mechanisms of detection, advantages and general strategies

In luminescent sensing of gases and vapors, the presence of a given analyte is detected through the modulation of luminescence from a probe material. This typically involves emission turn-on, emission turn-off, or shifts in the emission energy/wavelength from the luminescent probe. This type of sensing is advantageous in that it combines technical simplicity with the potential for extremely powerful performance. The instrumentation required only consists of an excitation source, probe material, emission detector, and signal output. The resulting devices can be extremely cost effective, and depending on the specific application, can often be compact enough for mobile use. Moreover, despite their low cost, small size, and ease of use, selective ppb-level sensitivity can be achieved through careful design of the probe material.

An effective luminescent probe should have short response time, good sensitivity and selectivity for the analyte, strong emission when in the on-state, high stability and reusability in real-world conditions. Because of their exceptional tunability, luminescent metal-organic frameworks (LMOFs) are especially effective in this role. Through the alteration of metal ions, organic ligands, guest molecules, and conditions used in synthesis, plus post-synthetic modification, nearly every physical and chemical quality of an LMOF can be tuned.

Porosity, pore geometries, and pore surface chemistry can be controlled to maximize selective interactions between the framework and the analyte material. This allows for the sensitivity, selectivity, and recyclability of the probe to be optimized. Simple adjustments of the pore dimensions allow for size-based selectivity. This can be accomplished by adjusting the actual pore size and geometry, or by partially occluding the pore through functionalization of the inner surface or the inclusion of guest molecules.⁴⁰ Similarly, controlling the chemical environment of the pore through ligand design, ligand functionalization, or specific guest inclusion can allow for the selection of species by their

chemical properties. Through the use of hydrophobic ligands, for example, hydrophilic molecules may be excluded from the pores of the material, further increasing its selectivity for a given hydrophobic analyte.⁴¹ In addition to tuning the broad chemical environment, specific functional groups that interact strongly with the desired analyte may be included in the pore to enhance selectivity for that material. Ligands with Lewis-basic moieties, such as amine-based functional groups, can be used to increase interactions with Lewis-acidic analytes.⁴² Post-synthetic removal of terminal ligands may expose open metal sites, allowing for the coordination of Lewis-basic analytes.⁴³ Ligands with large, planar, aromatic regions can increase π - π stacking interactions between the framework and aromatic analyte molecules.⁴⁴ These optimizations not only impact selectivity, but sensitivity as well. By improving the ability of an LMOF to selectively interact with the analyte material, pre-concentration of the analyte within the LMOF can be achieved.⁴⁵ This increases the local concentration of the analyte, allowing for extremely efficient sensing even when the general concentration of the analyte might otherwise be too low to detect.

LMOFs are also well suited as luminescent probe materials because of their favourable luminescence qualities. For example, in the cases of rigid frameworks built on organic chromophores, non-radiative excitation decay pathways can be significantly reduced compared with the chromophores in form of free molecules, resulting in LMOFs with extremely strong emission and quantum yields approaching unity.^{46, 47} Additionally, their multi-component design introduces a variety of potential emission mechanisms. In ligand-centered (LC) emission, excitation and emission processes are both located on a single ligand molecule, whereas ligand-to-ligand charge transfer (LLCT) involves the transfer of electron density from a donor ligand to an acceptor ligand upon excitation, with the reversal up emission. Similarly, metal-to-ligand charge transfer (MLCT) or ligand-to-metal charge transfer (LMCT) can occur, with the same movement of electron density from donor to acceptor upon excitation. Fluorescence resonance energy transfer (FRET) can also play a role in MOF luminescence. Excitation energy is first absorbed by a donor species — typically a ligand molecule — after which dipole-dipole interactions with the acceptor species — either another ligand or a metal — permits the non-radiative transfer of excitation energy from the donor to the acceptor. For this to occur, the donor must first possess an emissive transition with energy exactly matching that of an excitation transition in the acceptor, giving rise to spectral overlap between the emission of donor species and absorbance of acceptor species. Second, the dipole moments of the donor emission transition and acceptor excitation transition must be non-orthogonal. Following this energy transfer, the excited acceptor species emits.

A subclass of this energy transfer mechanism, or sensitization, forms the basis of emission in the expansive field of lanthanide-based LMOFs. Most trivalent lanthanide ions possess sharp, characteristic emission profiles, and they can be included either in the SBU or post-synthetically added to the

material's pores. However, as direct excitation of lanthanide ions requires parity-forbidden f-f transitions, their absorbance is extremely weak. To overcome this challenge, sensitizing ligands are used. Upon exposure to excitation energy, an electron is excited into the singlet excited state $S_{1,S}$ on the ligand, after which it undergoes intersystem crossing into the triplet excited state $T_{1,S}$ on the ligand. Energy transfer moves the excited state from the ligand $T_{1,S}$ to the emissive lanthanide triplet state $T_{1,A}$, where a photon is emitted.⁴⁸

Until now, these charge transfer and energy transfer mechanisms have been discussed as functioning between ligand molecules and metal ions. However, the inherent porosity of MOFs permits guest molecules within the pores to participate in these mechanisms as well. Guest molecules can act as independent luminescence centers, or they can participate in charge transfer to and from ligands or metals. Finally, multiple emission mechanisms can occur simultaneously within a single LMOF.

In designing an LMOF-based probe material to take advantage of these mechanisms, many options are available. As an analyte interacts with an LMOF it may induce changes in the emission wavelength, emission quenching, or emission enhancement. Shifting the emission energy occurs when interactions between the analyte and LMOF alter the LMOF electronic structure.⁴⁹ This can be accomplished through including functionality that directly interacts with the targeted analyte as described above. Additionally, it is possible to take advantage of vapochromic behavior in an LMOF, where the adsorption of polar or nonpolar molecules can stabilize or destabilize the excited state and thereby alter LMOF excited state energy levels and the wavelength of resulting emission.⁵⁰

The most common quenching mechanisms are charge transfer, in which a photoexcited electron is transferred from the higher-lying LUMO of the LMOF into the lower-lying LUMO of the (typically electron-deficient) analyte, and FRET, in which overlap between the emission spectra of the LMOF and absorbance spectra of the analyte permits transfer of excitation energy from the LMOF to the analyte, where it decays non-radiatively. While direct orbital overlap between LMOF and analyte molecules is required for charge transfer, FRET can take place over longer distances on the nanometer scale, and so requires only that the analyte be present in or near the LMOF's pore.⁴⁸ Emission enhancement can occur through a similar mechanism, with photoexcited electrons from the higher-lying analyte LUMO transferred into the lower-lying LMOF LUMO.

In either case, modulation of emission intensity from the LMOF requires specific relationships between the LUMO energy levels of the target analyte and LMOF, or spectral overlap between the LMOF emission and analyte absorbance. Using a chromophoric ligand-based strategy to prepare LMOFs with LC-based emission is useful method of designing an LMOF sensor with the appropriate LUMO energy levels or emission wavelength to interact with a targeted analyte.⁵¹ This strategy entails preparing an emissive ligand based on an organic chromophore with the optoelectronic properties and functionality necessitated by the target analyte, then

constructing it into a MOF with d^0 or d^{10} transition metals. These closed d subshell species have relatively low-lying HOMOs (highest occupied molecular orbitals) and high-lying LUMOs that usually preclude their participation in luminescence. The resulting MOF should then possess similar properties (emission and excitation spectra, HOMO and LUMO energy levels) as the initial chromophore.

Lanthanide LMOFs that participate in sensitized emission provide another lever by which an analyte can affect emission from the material. By interacting with the sensitizing ligand, an analyte can increase or decrease the efficiency of sensitization, leading to enhancement or quenching of emission from the emissive lanthanide.⁵² And while these strategies for preparing sensor materials are the most common, this is not an exhaustive list. Because of their great flexibility and tunability, creative researchers can induce changes in luminescence using any number of methods. Rationally designed materials that exhibit luminescence changes as a result of gas-adsorption-induced breathing have been reported,⁵³ as well as materials with emission turn-on when the adsorbed analyte displaced emission-quenching atmospheric O_2 .⁵⁴ Others have reported selective hydrogen-bonding analytes that rigidify unbound pendant functional groups and thereby enhance emission,⁵⁵ or the selective oxidation of an analyte species that results in enhanced emission from the LMOF.⁴⁵ Regardless, the exceptional properties of MOFs as luminescent probe materials promise that the rapid growth in the field will continue.

1.3. Design considerations of MOFs for the capture of hazardous gases and vapors

Adsorption related applications that make use of the porosity of MOFs are the most extensively studied areas among various aspects of MOF materials. MOFs are particularly promising for the capture and removal of target species because of their high porosity and tunability, which may not be readily achievable for traditional adsorbent materials.^{56, 57} This removal of the target species can be accomplished via bulk sequestration within the MOF structure followed by later desorption, or occasionally by the catalytic decomposition of the species within the MOF pore. The adsorption and decomposition of a target molecule has been extensively reported in the solution phase,⁵⁸⁻⁶⁰ and while it isn't as common in the vapor/gas phase, some examples do exist.⁶¹ However, as this review will primarily discuss and adsorption of toxic and hazardous gases, the decomposition of adsorbed species will not be a focus of this review.

To some extent, tailor-made MOFs with desirable pore shape, pore size, and surface functionality are attainable by design. For example, by applying reticular chemistry and ligand functionalization, one can fine-tune pore size and surface properties of MOFs for specific applications.⁶²⁻⁶⁴

The capture of hazardous gases and vapors commonly involves selective adsorption of target molecules from a mixture, usually under relatively low concentration. Within this context, various parameters including adsorption selectivity, uptake capacity, stability, recyclability, and cost should be

taken into consideration while evaluating the performance of an adsorbent candidate.

Firstly, it is important to note that adsorption selectivity and uptake capacity often have an inverse relationship, as selective adsorption is favored by relatively smaller pores for maximum size discrimination and/or sufficient adsorbate-adsorbent contact, while a high uptake capacity is typically favored by highly porous adsorbents.^{65,66} However this is not always the case, as both qualities also depend on the pore structure and surface functionality of the adsorbents, as well as the physical/chemical features of the adsorbates. For example, we recently reported the use of MIL-101-Cr based molecular traps for the capture of radioactive organic iodides from nuclear waste.⁶⁷ The tertiary amine functionalized MIL-101-Cr materials are able to selectively adsorb radioactive organic iodides with both high uptake capacity and selectivity, attributed to the high porosity of MIL-101-Cr and the tailor-made surface functionality which enables a specific interaction between the target adsorbate and the adsorbent. This example demonstrates how MOFs possessing high porosity and desirable functionality are advantageous for the capture of hazardous gases and vapors at low concentration. Thus, functionalization of existing, prototype materials represents an effective way to improve the capture performance.⁶⁸ For example, the amino-functionalized MOF-5 and hydroxyl-functionalized MOF-205 show substantially enhanced ammonia capture capability compared to their parent compounds, owing to the formation of strong hydrogen bonds between ammonia and functional groups from the adsorbents.^{69,70} The same strategy has proven effective for the capture of SO_x, NO_x, H₂S etc.⁷¹

Stability (both thermal and chemical stability) is another crucial factor that influences the performance of an adsorbent material. It has commonly been neglected in the early exploration of MOFs, especially with regards to water/chemical stability. It has been shown that the gas capture capability of MOFs may drop significantly under real-world systems or simply in the presence of moisture, despite previous adsorption measurements performed under dry conditions that indicate very high performance.⁷² But over the past few years, the stability of MOFs has been greatly enhanced through the use of high valence metals such as zirconium, aluminum, and yttrium.⁷³⁻⁷⁵ Some of these MOFs have exhibited exceptional framework robustness which can be thermally stable up to 400+ °C and retain their crystallinity and porosity in hot water or even in acidic or basic solutions.⁷⁶ Additionally, the introduction of hydrophobic linkers can improve the water stability of MOFs, and with the added benefit of depressing the competitive adsorption of moisture.⁷⁸⁻⁸⁰

Recyclability, which is normally correlated with cost, must also be taken into account when considering an adsorbent material for industrial implementation. MOFs are typically reusable in cases where the capture process involves only physisorption without altering the integrity of the adsorbent. When chemisorption is involved, the adsorbent is usually unrecyclable. However, it has been shown that chemisorbed

species may be fully desorbed under optimized conditions, making the adsorbent recyclable.⁸¹ Additionally, for post-synthetically functionalized MOFs, it is possible to remove the chemisorbed adsorbates together with the functional moieties and reuse the original adsorbents.⁶⁷

Finally, the cost of a MOF is usually dominated by the organic linker used, as the most common MOF node metals (Zn, Cu, Zr, Al etc.) are earth abundant and inexpensive. Thus, for real-world applications, low cost and readily available ligands, rather than those synthesized through complicated organic reactions, are favorable.

2. Detection of harmful gases and vapors by LMOFs

Pollution of the air, soil, and water is a global issue, with diseases resulting from pollution responsible for 9 million premature deaths in 2015, or 16% of all deaths worldwide.⁸² The treatment of pollution-related costs is also a burden on health systems, with welfare losses due to pollution accounting for 6.2% of global economic output.⁸² Pollution of the atmosphere by gas and vapor-phase chemical species is contributes the majority of this risk, with approximately 7 million deaths attributable to air pollution in 2012.⁸³ Industrial and power plant exhaust streams, vehicle exhaust, outgassing from materials, and improper waste disposal all play key roles in introducing these harmful species into the atmosphere, and monitoring their concentration is a key component of any assessment of air quality. Additionally, the detection of specific gasses and volatile compounds is of use in industrial safety monitoring. LMOFs provide an excellent opportunity to develop new, cost-effective alternatives to existing detection methods.

2.1 Detection of aromatic VOCs

Aromatic VOCs include species like benzene, toluene, nitroaromatic species, aromatic amines like aniline, and many other compounds. They are commonly used in myriad ways by various industry, from solvents and coatings to pesticides, medicinal precursors, packaging, and building materials. Vehicle exhaust is another common source of aromatic VOCs. Some, such as benzophenone or benzaldehyde, have limited toxicity and are commonly used as flavoring agents or in soaps. Others, like benzene, are acutely toxic and carcinogenic.⁸⁶ Exposure to hazardous aromatic VOCs can be an occupational hazard for employees working in industries that employ them and an environmental hazard for those living or working near waste-disposal sites. Exposure can also arise via outgassing of the aromatic VOC from building materials such as particleboard or flooring adhesives.⁸⁷

Nitroaromatic compounds (NACs) were among the first class of VOCs to be detected in the vapor phase by LMOF materials. In 2009, we reported Zn₂(bpdC)₂(bpee) (bpdC = 4,4'-biphenyldicarboxylate, bpee = 1,2-bipyridylethene), a porous and strongly LMOF with blue emission.^{88,89} In the presence of dinitrotoluene (DNT) or nitrobenzene (NB) vapors at

approximately 0.18 ppm and 300 ppm, respectively, emission from the LMOF was strongly and rapidly quenched, with an 85% reduction in luminescence intensity following a 10 second exposure (figure 1). This was accomplished through a redox quenching mechanism. Following photoexcitation, excited LMOF electrons were transferred from the lowest unoccupied molecular orbital (LUMO) of the LMOF into the lower-lying LUMO of the electron-deficient nitroaromatic compound, quenching emission from the LMOF. This sensing behavior was fully reversible by heating the sensor LMOF at 150 °C for about one minute (figure 1).

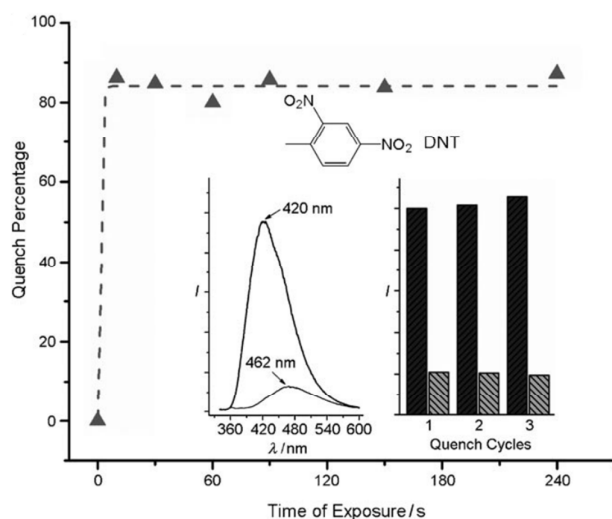


Figure 1. Graph showing the emission quench percentage vs time for the LMOF $Zn_2(bpdc)_2(bpee)$ following exposure to DNT vapors. The structure of DNT is inset, along with the LMOF's emission spectra before exposure (emission peak at 420 nm) and after exposure (emission peak at 462 nm). Recyclability tests are also inset, showing the intensity of emission before (dark grey) and after (light grey) exposure to DNT vapors over several cycles.⁸⁸ Reproduced from ref. 88 with permission from the John Wiley & Sons, Inc, copyright 2009.

A follow-up work of ours introduced the ability to identify the analyte through the use of 2D signal modulation, with exposure to different analyte NACs altering both emission intensity and emission wavelength to different degrees.⁹⁰ The LMOF $Zn_2(ndc)_2(bpe)$ ($ndc = 2,6$ -naphthalenedicarboxylate, $bpe = 1,2$ -bis(4-pyridyl)ethane) was exposed to vapors of NB, 2-nitrotoluene (mNT), 1,3-dinitrobenzene (mDNB), 2,4-dinitrotoluene (2,4-DNT), 1,4-dinitrobenzene (pDNB), and 2,4,6-trinitrotoluene (TNT), in addition to a number of other solvent molecules. Following a 5-minute exposure, emission from the LMOF was quenched by 45 – 95% and blueshifted by 2 – 25 nm, depending on the analyte in use. Molecular loading simulations and DFT calculations were used to demonstrate that the strength of interaction between the analyte and framework was responsible for the degree of emission blue shift.

As discussed earlier, improving the stability of LMOF sensor materials in the presence of moisture was a vital requirement for real-world application. An example of a moisture-stable LMOF able to detect NAC vapors was reported in 2015 by Zang and Hou *et. al.*⁹¹ using the metal ion Tb^{3+} . When exposed to NB

and mNT vapors, the characteristic Tb^{3+} emission from the LMOF $Tb(L)(OH)$ ($L = 5$ -(4-carboxyphenyl)pyridine-2-carboxylate) was quenched. Emission from the LMOF in the absence of analyte followed the standard mechanism for sensitized lanthanide systems—excitation of the ligand singlet state, followed by intersystem crossing into the ligand excited triplet state, and finally energy transfer to the lanthanide triplet state that resulted in characteristic lanthanide emission. However, in the presence of NACs, the initial excited electron was instead transferred from the ligand singlet state into the lower-lying LUMO of the electron deficient analyte, quenching emission from the LMOF.

Aromatic amines are another aromatic VOC pollutant with significant health hazards. While most vapor-phase NAC detection involves π - π interactions between the analyte and framework, the amine group present in aniline and other aromatic amines provides an additional target for interaction. An example of an LMOF with hydrogen-bond acceptor moieties for aniline detection was reported in 2014 by Zhao and Li *et. al.*⁹² The cadmium-based LMOF $[CdL] \cdot [H_2N(CH_3)_2]^+(DMF)(H_2O)_3$, synthesized using the amide-containing ligand bis(3,5-dicarboxyphenyl)terephthalamide (H_4L), emits strong blue light at 450 nm through a ligand-centered emission process. Following exposure to aniline vapors, emission from the LMOF was quenched by 15% after 200 seconds, with the majority of the quenching occurring after only 25 seconds. The authors ascribe interaction between the LMOF and the aniline vapor to both π - π interactions between the aromatic moieties on the ligand and analyte and hydrogen bonding between the aniline amine hydrogen and the amide group in the ligand molecule.

Amine basicity also provides a method of amine-specific sensing, as demonstrated by Lin and Huang *et. al.*⁴⁴ The electron-poor ligand DPNDI (N,N'-di(4-pyridyl)-1,4,5,8-naphthalene diimide) was first reacted with $AnSiF_6$ clusters to produce a weakly emissive LMOF, which was then loaded with electron-rich naphthalene guests to create $1a \supset naphthalene$. This guest-loaded LMOF fluoresced brightly at 600 nm due to an exciplex electronic charge transfer state between the electron-rich and the electron-poor framework ligand. When $1a \supset naphthalene$ was exposed to basic vapors, in addition to a number of aliphatic amines, electron transfer from the strongly basic vapor to the π -acidic ligand interrupted the emissive charge transfer mechanism and quenched emission. The interruption of the exciton formation also resulted in a clear color change (figure 2). Finally, the guest-loaded LMOF also demonstrated some size preference, with the bulkiness of the amine inversely related to the strength of the quenching interaction.



Figure 2. Color change induced in **1a**-naphthalene when exposed to amine vapors.⁴⁴ Reproduced from ref. 44 with permission from the American Chemical Society, copyright 2016.

While the majority of luminescent sensors exhibit emission turn-off in the presence of a given analyte, emission turn-on is also possible, and is often preferred as it is less susceptible to false positive signals related to device malfunction. As quenching is often observed in cases of electron-deficient analytes with LUMO energy levels below that of the sensor LMOF, emission enhancement can occur in electron-rich analytes with LUMO energy levels above that of the LMOF sensor. We reported an early example of this interaction in 2011, with the LMOF $Zn_2(\text{oba})_2(\text{bpy})$ (oba = 4,4'-oxybis(benzoic acid), bpy = 4,4'-bipyridine).⁹³ While it demonstrated emission quenching in the presence of NAC vapors, the LMOF emission at 420 nm was enhanced in the presence of electron-rich aromatic VOCs benzene (80% enhancement), chlorobenzene (70% enhancement) and toluene (120% enhancement) (figure 3). The degree of increase in emission intensity was in trend with the electron density in the benzene ring, and DFT calculations indicated that the LUMO of these three analytes was indeed higher than that of the LMOF. Cyclic voltammetry measurements showed that the reduction potential of the three analytes were more negative than the LMOF, indicating that the LMOF would act as an electron acceptor. Our subsequent studies have shown such electron transfer is a very common process observed in MOFs.⁹⁴⁻⁹⁶

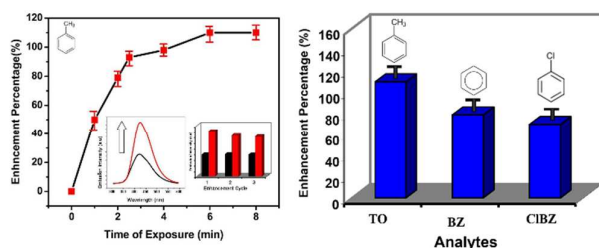


Figure 3. (a) Enhancement of emission from the LMOF $Zn_2(\text{oba})_2(\text{bpy})$ following exposure to toluene v. time of exposure, with before/after exposure emission spectra and recyclability chart inset. (b) Enhancement of LMOF emission in the presence of toluene (TO), benzene (BZ), and chlorobenzene (CIBZ) vapor.⁹³ Reproduced from ref. 93 with permission from the American Chemical Society, copyright 2011.

A similar sensor for benzene with a much stronger response was recently reported by Lan and Sun *et al.*⁹⁷ The porous cadmium-based LMOF has the formula $Cd_3(L)(\text{bipy})_2 \cdot 4H_2O$ (H6L = tri-((4-carboxyphenoxy)methyl)methoxy)-tri-((4-carboxyphenoxy)methyl)methane) and exhibits approximately an 8-fold increase in luminescence intensity when exposed to benzene vapors with a response time of less than one minute. The LMOF fluoresces at 381 nm under 314 nm excitation through a ligand-to-ligand charge transfer process. DFT calculations indicated that the lowest unoccupied molecular orbital (LUMO) of the LMOF was primarily located on the aromatic bipy ligand. These calculations also indicated that the LUMO of benzene is slightly higher than the LUMO of the LMOF, allowing energy transfer from benzene to the LMOF

LUMO to enhance the emission intensity. Exposure to nitrobenzene, conversely, caused a strong quenching response, as calculations showed the LUMO of nitrobenzene to be lower than that of the LMOF, resulting in energy transfer out of the excited LMOF LUMO and into that of nitrobenzene, as in previous examples (figure 4).

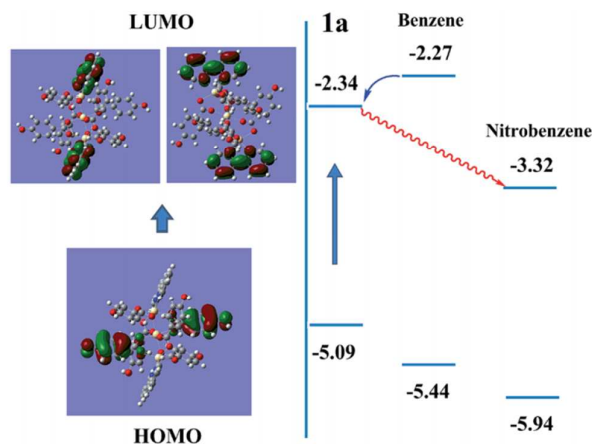


Figure 4. (left) Representative fragment of the LMOF $Cd_3(L)(\text{bipy})_2 \cdot 4H_2O$ used in DFT calculations, with molecular orbitals corresponding to the fragment HOMO and LUMO shown. (right) Schematic demonstrating the relative positions of the calculated LMOF fragment, benzene, and nitrobenzene HOMOs and LUMOs, as well as the proposed mechanism of emission quenching or enhancement.⁹⁷ Reproduced from ref. 97 with permission from the Royal Society of Chemistry, copyright 2015.

2.2 Detection of aliphatic VOCs

Aliphatic VOCs are another class of common atmospheric pollutant, with anthropogenic sources accounting for the emission of approximately 142 million metric tons of VOC carbon per year.⁹⁸ Much like aromatic VOCs, these compounds are widely used as solvents or additives in paints, coatings, polymers, building materials, office equipment, and fuels. They typically enter the atmosphere through evaporation, outgassing, or following the incomplete combustion of fossil fuels. Atmospheric VOC levels have been shown to be elevated 2-5 fold in indoor residential spaces when compared to outdoor spaces, regardless of the rural or urban location of the space, with some aliphatic VOCs posing serious health risks. In industrial settings that utilize these VOCs, the levels of exposure can be even higher.

Yan and Xu reported an interesting LMOF composite material for the sensitive and selective determination of aliphatic aldehyde vapors, with the specific application of detecting aldehyde pollution in automobiles.⁴⁵ 10 nm ZnO nanoparticles were prepared, then reacted with $ZrCl_4$ and $H_2\text{bpydc}$ (2,2'-bipyridine-4,4'-dicarboxylic acid) to form a UiO-66-type MOF (UiO-MOF) around the ZnO nanoparticles, which was confirmed by TEM and spectroscopic studies. The resulting $ZnO@UiO-MOF$ (ZUM) composite material was then loaded with Eu^{3+} post-synthetically to generate $Eu@ZUM$, with the Eu^{3+} atoms coordinated to the bipyridine moiety of the bpydc ligands. Under 365 nm excitation, emission from $Eu@ZUM$ was a mix of ligand-centered emission at 470 nm

and Eu-centered emission at 590, 614, and 700 nm, with the intensity at 614 nm:the intensity at 470 nm (I_{614}/I_{470}) = 2.3. The Eu@ZUM was mounted onto a strip of test paper and exposed to a series of vehicle cabin pollutants, including formaldehyde (FA) benzene (Ben); ortho-, meta-, and para-xylene (OX, MX, and PX); ethylbenzene (EB); butyl acetate (BA); toluene (Tol); and cyclohexane (CH). The resulting I_{614}/I_{470} was 2.3 ± 0.1 for all analytes except FA, which had $I_{614}/I_{470} = 5.5$ (figure 5). Subsequent trials with larger aldehydes acetaldehyde (AA) and acraldehyde (ACA) also gave elevated I_{614}/I_{470} of 4.3 and 3.3, respectively. Additionally, the linear relationship between the concentration of FA vapor and I_{614}/I_{470} permitted the authors to calculate a limit of detection (LOD) of 42 ppb for FA at 25 C. Finally, the authors demonstrated that the sensing was completely reversible by removing the test paper from the FA-containing atmosphere. When investigating the sensing mechanism, it was found that the lifetime of the Eu-centered emission at 614 was unchanged in the presence of FA; the authors therefore ruled out direct interaction between FA and Eu^{3+} . Additionally, since the intensity of the ligand-centered emission at 470 nm was consistent with the other analytes (figure 5), the authors ruled out some interaction between FA and bpydc that increased the efficiency of sensitization. Instead, it was determined that increased electron density in the valence band of the ZnO nanoparticles within Eu@ZUM — caused by energy transfer from the excited UiO-MOF to the ZnO nanoparticles—ionizes preadsorbed molecular oxygen, which oxidizes the aldehyde analyte molecule, with the emancipated electrons being injected into the Eu^{3+} excited state and resulting in enhance emission.

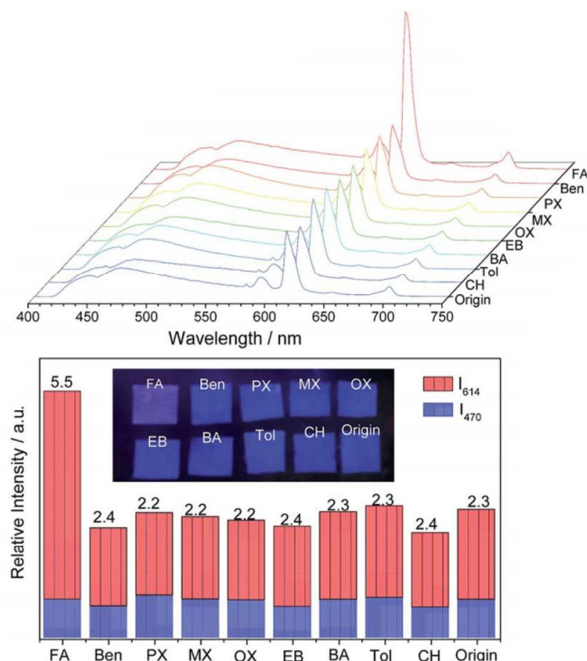


Figure 5. (top) Emission spectra of Eu@ZUM under 365 nm excitation when exposed to VOC pollutant vapors. (bottom) Relative intensity of emission from Eu@ZUM at 614 nm compared to emission at 470 nm when exposed to pollutant vapors, with an image of the test strips illuminated by 365 nm UV light inset. Abbreviations: FA = formaldehyde,

Ben = benzene, PX = para-xylene, MX = meta-xylene, OX = ortho-xylene, EB = ethylbenzene, BA = butyl acetate, Tol = toluene, CH = cyclohexane, Origin = native Eu@ZUM.⁴⁵ Reproduced from ref. 45 with permission from the Royal Society of Chemistry, copyright 2017.

A pair of LMOFs able to detect both amine and aldehyde vapors was reported in 2016 by Yang, Song, and Ma *et al.*¹⁰⁰ Both LMOFs used an unusual chair-conformation resorcin[4]arene-based octacarboxylate ligand H_8L , with **1** having the formula $[\text{Cd}_2(\text{L})][(\text{CH}_3)_2\text{NH}_2]_4 \cdot 4\text{H}_2\text{O}$ and **2** having the formula $[\text{Zn}_2(\text{L})][(\text{CH}_3)_2\text{NH}_2]_4 \cdot 2\text{DMF} \cdot 4\text{H}_2\text{O}$. Both exhibited blue-green ligand-based emission, which was quenched following short exposure to amine and aldehyde vapors. Each LMOF was exposed to formaldehyde, ethanal, propanal, butanal, pentanal, hexanal, and benzaldehyde vapors, as well as ammonia, ethylamine, diethylamine, trimethylamine, propylamine, butylamine, and aniline vapors. In the case of aldehyde vapors, the same trend was observed in both **1** and **2**, with formaldehyde causing the lowest quenching amount with approximately 15% and 10% reduction in emission intensity respectively. The quenching amount increased in trend with molecular weight, and benzaldehyde caused the strongest quenching at about 48% and 80% for **1** and **2**, respectively. In all cases, there was no shift in the ligand-centered emission. The higher sensitivity for benzaldehyde in **2** was attributed to its slightly larger channels, which loading simulations indicated could accommodate 2 benzaldehyde molecules per unit cell, unlike the single benzaldehyde per unit cell of **1**. Unlike benzaldehyde, the amine vapors induced both emission quenching and red- and blue-shifted emission from both **1** and **2**. In each case, aniline caused the strongest emission quenching accompanied by a small redshift, while ammonia induced moderate quenching and a 25 nm blueshift, and ethylamine caused similarly moderate quenching accompanied by a redshift of 40 nm in **1** and 20 nm in **2**. This combination of altered emission wavelength and variable quenching efficiency allowed the authors to construct a 2D map of quench % v. emission shift, potentially permitting the identification of amine vapors through a specific interaction with the sensor LMOFs (figure 6).

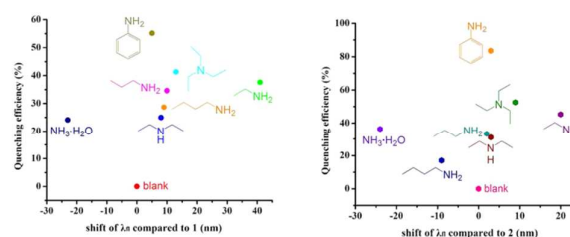


Figure 6. 2D map of quenching efficiency v. emission wavelength shifts of **1** (left) and **2** (right) when exposed to amine vapors.¹⁰⁰ Reproduced from ref. 100 with permission from the American Chemical Society, copyright 2016.

An LMOF displaying strong emission turn-on in the presence of aliphatic amines was recently reported that takes advantage of specific interactions between a hydrogen bonding pocket and the low-weight amines methylamine, dimethylamine, and trimethylamine.¹⁰¹ In the two-dimensional

strontium-based $\text{Sr}(\text{H}_2\text{ABTC})(\text{DMF})(\text{H}_2\text{O})$ ($\text{H}_2\text{ABTC} = 3,3,5,5$ -azobenzenetetracarboxylic acid), two of the four carboxyl groups in the ABTC ligand are non-coordinating and remain protonated. Two of these carboxyl groups from neighboring ligands, plus one water molecule coordinated to a neighboring Sr^{2+} , form a hydrogen-rich pocket. Upon introduction of methylamine, dimethylamine, or trimethylamine vapor, hydrogen bonding between this pocket and the amine rigidifies the structure (figure 7). Under 10 ppm exposure, this results an approximately two-fold increase in the emission intensity from the LMOF, as well as a redshift in peak emission energy from 558 to 610 nm (figure 7). The authors report that the limit of detection is on the order of 10 ppb at room temperature, making this material a promising visual sensor for amine vapors.

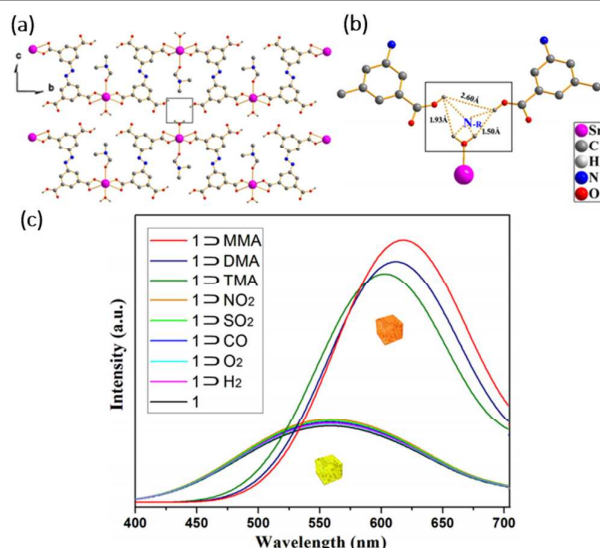


Figure 7. (a) Two neighboring 2D sheets of $\text{Sr}(\text{H}_2\text{ABTC})(\text{DMF})(\text{H}_2\text{O})$, viewed from within the plane of the sheet. (b) Detail of the H-bonding pocket formed between two sheets, with the approximate location of the amine analyte shown. (c) Emission spectra of $\text{Sr}(\text{H}_2\text{ABTC})(\text{DMF})(\text{H}_2\text{O})$ in the presence of 10 ppm methylamine (MMA), dimethylamine (DMA) and trimethylamine (TMA), as well as nitrogen dioxide, sulfur dioxide, carbon monoxide, and hydrogen gas.¹⁰¹ Reproduced from ref. 101 with permission from the John Wiley & Sons, Inc, copyright 2017.

Another material exhibiting selective emission turn-on in the presence of amine vapors was reported by Mandal *et al.*¹⁰² The material $\text{Zn}(\text{PA})(\text{BPE})$ (PA = pamoic acid, bpe = 1,2-bis(4-pyridylethane)) is composed of a three-dimensional framework with 5-fold interpenetration, in which dipole-dipole interactions between amine vapors of ethylenediamine, diisopropylamine, hydrazine, and *n*-butylamine lead to emission enhancements of 30 – 100%, with the strength of emission enhancement in trend with the dipole moment of the amine vapor. The material shows no response to a number of other polar and non-polar solvent vapors, and DFT calculations indicate that the higher-lying LUMO of the amines inject electrons into the lower-lying LUMO of $\text{Zn}(\text{PA})(\text{BPE})$ upon photoexcitation, resulting in the increased emission intensity from the sensor material.

A turn-on sensor for the widely used aliphatic amide dimethylformamide (DMF) was reported which exhibits an emission enhancement of more than eight fold in the presence of DMF vapor.¹⁰³ The lanthanide-based LMOF $\text{Eu}_2\text{L}_3(\text{H}_2\text{O})_4 \cdot 3\text{DMF}$ (**1**, L = 2',5'-bis(methoxymethyl)-[1,1':4',1''-terphenyl]-4,4''-dicarboxylate) was synthesized solvothermally in DMF and showed strong Eu-centered luminescence. **1** was then soaked in water for three days to give **2**, with all remaining DMF molecules exchanged with water. **2** exhibited much weaker luminescence than **1**, as the O-H bond vibrations are known to quench emission from Eu^{3+} .¹⁰³ Upon exposure to a variety of solvent vapors, the luminescence was slightly enhanced (up to 150%), with the enhancement primarily due to the displacement of water molecules within the pore, preventing the quenching of Eu^{3+} emission. However, upon exposure to DMF vapor, emission intensity was enhanced eight-fold (figure 8). The selectivity for DMF was attributed to the fact that the initial solvothermal synthesis of the LMOF took place in DMF. As a result, DMF molecules acted as solvent templates during the synthesis of the material, allowing DMF molecules from the vapor to fit into tailored spaces within the LMOF. These close interactions between the DMF and the LMOF ligands shift the excited state energy in the ligand to increase sensitization of the emissive Eu^{3+} centers, resulting in turn-on emission.

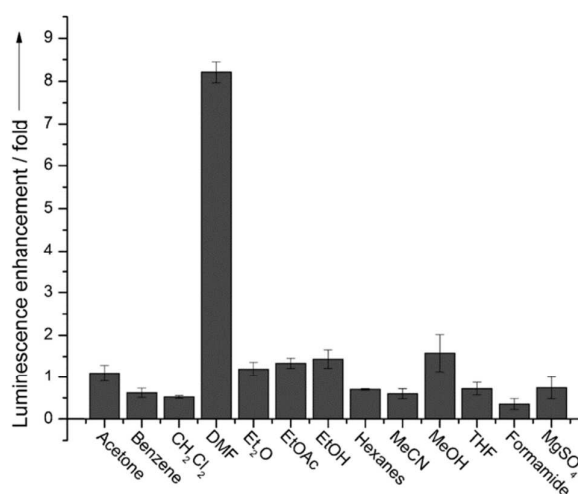


Figure 8. Emission intensity enhancement of **2** upon incubation in a closed vial with a variety of solvent vapors. MgSO_4 was included in one vial as a desiccant, to show that removal of water from **2** resulted in emission turn-on. Reproduced with permission from reference¹⁰³ Reproduced from ref. 103 with permission from the John Wiley & Sons, Inc, copyright 2013.

The detection of aliphatic thiols was reported in 2013, through the use of an Eu^{3+} -loaded LMOF film.⁴³ Films of In-BTC (btc = 1,3,5-benzenetricarboxylate) were prepared solvothermally on a Si wafer that was coated with Pt nanoparticles, which served to increase the roughness of the surface and improve MOF nucleation. The resulting MOF possessed MIL-100-type connectivity, with two of the BTC carboxylates coordinating with In^{2+} while the third projected uncoordinated into the pore. Eu^{3+} was postsynthetically added

to the material at a ratio of $\text{Eu}:\text{In} = 0.071$ to create $\text{In-BTC}\supset\text{Eu}$, with the added Eu^{3+} coordinated to the free carboxylate group. The resulting $\text{In-BTC}\supset\text{Eu}$ thin film showed characteristic Eu^{3+} emission with peak emission intensity at 618 nm. The excitation spectrum at 618 nm emission showed a broad band between 200–300 nm corresponding to absorbance by the btc ligand, demonstrating that the lanthanide was efficiently sensitized. Upon exposure to saturated vapors of 1-butanethiol and 1,2-ethanedithol, emission was quenched by 94% within 20 seconds and 92% within 120 seconds for each analyte respectively. The authors claim that the emissive Eu^{3+} within the LMOF pores was coordinatively unsaturated, allowing the thiols to bind with open sites on the metal and quench emission.

A porous $\text{Cu}(\text{I})$ -based LMOF ($\text{H}_2\text{O}\supset\text{Cu}_2(\text{L})_2\text{I}_2$, $\text{L} = 1$ -benzimidazolyl-3,5-bis(4-pyridyl)benzene) able to detect the presence of small halocarbons on the ppm level through an emission turn-on was reported by Dong *et al.*⁵⁵ When exposed to CHCl_3 and CH_2Cl_2 , emission from the material turned on, with a two-fold increase in intensity and a slight blueshift. For both analyte molecules, the authors report a limit of detection of 10 ppm. In order to identify the mechanism of this emission enhancement, $\text{H}_2\text{O}\supset\text{Cu}_2(\text{L})_2\text{I}_2$ was incubated in the analyte solvents, and single crystal analysis was able to locate the adsorbed solvent molecules within the pore. Instead of coordinating with the metal ions, CHCl_3 and CH_2Cl_2 were found to form weak hydrogen-bonding interactions with the ligand molecule. The analyte-loaded sample was also found to have a slightly blueshifted absorbance band. The authors propose that the hydrogen bonds serve to rigidify the LMOF structure and alter ligand energy levels, making the emission more efficient.

A LMOF was constructed by linking a luminescent dodecanuclear silver chalcogenide cluster $[(\text{Ag}_{12}(\text{S}^t\text{Bu})_6(\text{CF}_3\text{COO})_6(\text{CH}_3\text{CN})_6)]\cdot\text{CH}_3\text{CN}$ (**Ag₁₂**) into a framework with bpy (4,4'-bipyridine) ligands replacing the previously coordinating CH_3CN groups.⁵⁴ The resulting LMOF **Ag₁₂bpy** ($\text{Ag}_{12}(\text{StBu})_8(\text{CF}_3\text{COO})_4(\text{bpy})_4$) gave strong green emission at 500 nm in the absence of O_2 , but in the presence of O_2 , emission was strongly quenched. However, when exposed to a group of VOC solvent vapors including chloroform, emission from **Ag₁₂bpy** was turned on again through a fast displacement mechanism with response in under one second, as VOC molecules replaced O_2 within the material's pores (figure 9X). Additionally, the position of the emission peak redshifted by up to 50 nm based on the identity of the VOC adsorbed, with chloroform inducing a redshift of approximately 25 nm (figure 9), thus allowing the identification of the VOC vapor. Both adsorption data and single crystal analysis confirmed that an average of four chloroform molecules were present per unit cell.

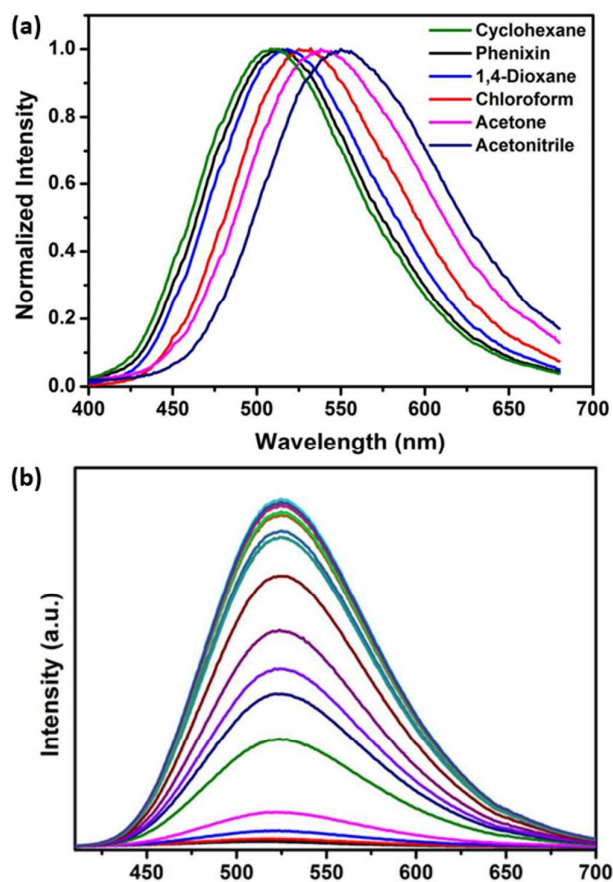


Figure 9. (a) Shift in emission from **Ag₁₂bpy** when exposed to various VOC vapors. (b) Emission turn-on in **Ag₁₂bpy** when exposed to increasing concentration of CHCl_3 vapors.⁵⁴ Reproduced from ref. 54 with permission from the Nature Publishing Group, copyright 2017.

2.3 Toxic and hazardous gas detection

Pollution resulting from combustion exhaust is the largest source of exposure to hazardous gases, include CO , NO , NO_2 , and SO_2 . These compounds are acutely toxic, and in the case of NO_2 and SO_2 , are contributors to acid rain. Other toxic gases, like HCl , can be produced by burning plastics or other polymers. Ammonia vapor is among the most common indoor pollutants, and can be released from cleaning products or outgas from building materials.¹⁰⁶ Detecting these and other harmful gases and vapors is an important aspect of air quality monitoring; however, when compared with aromatic and aliphatic VOCs, relatively fewer LMOFs have been reported for the detection of these species. While ammonia detection is fairly well developed, the LMOF-based detection of many other common hazardous gases including SO_2 or CO have not been reported, to the best of our knowledge.

A LMOF based on UiO-66 ($\text{Zr}_6\text{O}_4(\text{OH})_4(\text{bdc})_6$, $\text{bdc} = \text{benzene-1,4-dicarboxylate}$) able to detect the toxic gases NO , NO_2 , and Br_2 was reported in 2015 by Kaskel *et al.* which targets these three gases by their ability to act as strong oxidizers.¹⁰⁷ By postsynthetic modification, dihydro-1,2,4,5-tetrazine-3,6-

dicarboxylate (dhtz) ligand molecules replaced bdc ligands within the structure of UiO-66 at approximate a 5:1 bdc:dhtz ratio to give UiO-66(dhtz). This dihydro-1,2,4,5-tetrazine unit was chosen for its ability to be easily oxidized to 1,2,4,5-tetrazine (tz), and for the fact that this oxidation results in a clear colorimetric shift from yellow to pink as a result of increased blue-green light absorbance. Upon exposure to NO, NO₂, and Br₂ gas, the dhtz ligands within UiO-66(dhtz) were oxidized to tz, giving UiO-66(tz) and a clear color change from yellow to pink (figure 10). This oxidation could be fully reversed by suspending UiO-66(tz) in an aqueous solution with the reducing agent sodium dithionite, allowing the material to be used again. PXRD and gas adsorption measurements demonstrated that the structure's crystallinity and porosity was not affected by the postsynthetic ligand replacement, oxidative sensing, or reductive regeneration.

clear spectral and colorimetric change with the extremely low limit of detection of is 2.4 ppm NH₃, which is well below the 50 ppm workplace limit.¹⁰⁸ The response was also rapid, with the first change by 30 seconds and a complete response after 240 seconds. Furthermore, the material can be regenerated and reused by simple exposing the material to ambient air (figure 11). As the PXRD and Eu-centered emission lifetime of the LMOF is unchanged, the structure is stable in the presence of the analyte, and the analyte does not interact directly with the Eu³⁺ ion. Instead, the analyte interacts with the ligand. IR peaks of ligand skeleton shift when exposed to analyte, and ligand absorbance increased, along with a 24 nm redshift in ligand emission, indicating that H-bonding between the ligand and analyte lowered the ligand π* orbitals. This prevented effective sensitization of the Eu, and resulted in the observed signal.

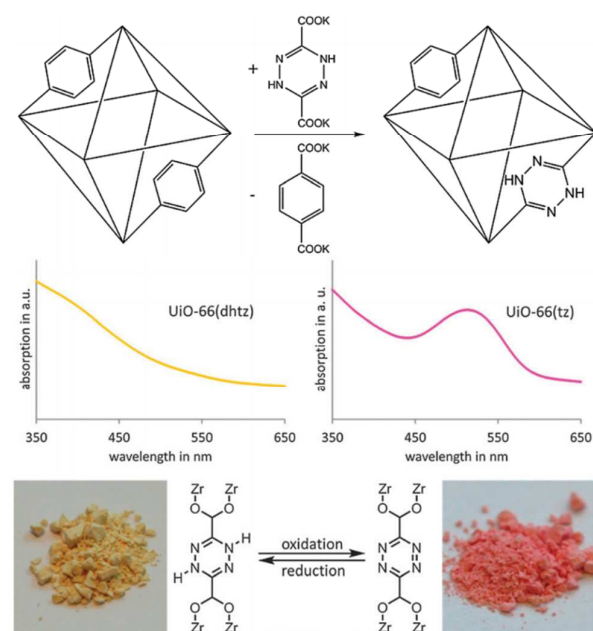


Figure 10. (top) Postsynthetic ligand replacement of bdc with dhtz to give UiO-66(dhtz). (bottom) The fully-reversible oxidation of UiO-66(dhtz) to UiO-66(tz) in the presence of NO, NO₂, or Br₂ gases.¹⁰⁷ Reproduced from ref. 107 with permission from the Royal Society of Chemistry, copyright 2015.

A nanocrystalline, lanthanide-based LMOF has been reported for the sensitive, selective detection of ammonia vapor with the detection giving both a photoluminescent and a colorimetric signal.¹⁰⁸ Nanocrystalline Ga(OH)bpydc (2,2'-bipyridine-4,4'-dicarboxylic acid) was prepared solvothermally, with Eu³⁺ emission centers added postsynthetically. These Eu³⁺ ions coordinate with the bipyridine moiety of the ligand, resulting in efficient sensitization and Eu-centered emission from the LMOF. When exposed to a number of indoor air pollutants including benzene and formaldehyde vapors, there is very slight emission enhancement or quenching—on the order of ±5-10%. However, when exposed to NH₃ a 76% quench of Eu-based emission was observed, coupled with strong enhancement of ligand-based emission. This led to a

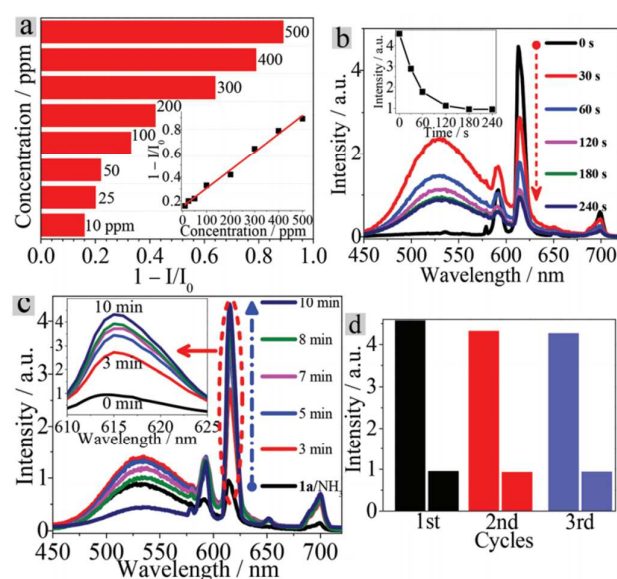


Figure 11. (a) Intensity of emission from Eu@Ga(OH)bpydc under different concentrations of NH₃ vapor. (b) Emission spectra of Eu@Ga(OH)bpydc following exposure to NH₃ vapors at various exposure times, with the emission intensity at 614 nm v. time inset. (c) Emission spectra of Eu@Ga(OH)bpydc following exposure to ambient air, demonstrating the recovery of luminescence, with the peak at 614 nm inset. (d) Intensity of the 614 nm emission from Eu@Ga(OH)bpydc before (left) and after (right) exposure to NH₃ vapors over three cycles.¹⁰⁸ Reproduced from ref. 108 with permission from the Royal Society of Chemistry, copyright 2016.

Ammonia was also detected selectively at high temperatures through interactions with Zn²⁺ and Mg²⁺ open metal sites (OMS) in Zn₂(tcpe) (tcpe = tetrakis(4-carboxyphenyl)ethylene) and Mg(H₂DHBDC) (H₂DHBDC²⁻ = 2,5-dihydroxybenzene-1,4-dicarboxylate), respectively, that induced a significant redshift in emission from the LMOFs.¹⁰⁹ The behavior was first noted in Zn₂(tcpe), which forms paddlewheel SBUs with four ligand carboxylates forming the paddles and two water molecules coordinating in the axial positions. At room temperature, emission from the material redshifts when exposed to NH₃, triethylamine, and ethylene diamine, but once heated to 100 °C, redshifted emission is only observed when the material is exposed to NH₃. DFT calculations demonstrated that this was

likely because of the interactions between NH_3 and the OMS on Zn following removal of the coordinating water are stronger than interactions between other analytes and the Zn^{2+} OMS. However, this interaction was also accompanied by an irreversible structure change as observed in PXRD. This led the authors to consider $\text{Mg}(\text{H}_2\text{DHBDC})$, as it likewise possessed coordinating solvent that could be removed under heating and maintained emission intensity at elevated temperatures. Upon exposure to NH_3 vapor at 100°C , redshifted emission was again observed from the MOF. However, as the interaction between NH_3 and Mg^{2+} isn't as strong as the interaction between NH_3 and Zn^{2+} , the coordinated ammonia could be removed by evacuation for 15 minutes, allowing the sensor material to be reused.

A Eu^{3+} -based 1D coordination polymer that stacks to form a 3D porous network was used to detect gaseous HCl through the protonation of a non-coordinative basic site on the ligand.⁵² In the $\text{EuH}(\text{L})_2(\text{NO}_3)_2$ (**EuL**, $\text{L} = 2$ -(2-pyridin-2-yl)quinoline-4-carboxylic acid) is composed of an infinite PBU, with each Eu^{3+} center coordinated to carboxylate groups from four ligand molecules plus two NO_3^- ions, with each carboxylate group bridging two Eu^{3+} ions to form a 1D chain. **EuL** emits characteristic Eu^{3+} -centered emission with efficient sensitization by the ligand. However, in the presence of HCl gas, the free pyridine moieties are protonated, and emission from the material is quenched. Time-dependent Hartree-Fock calculations were performed to determine the energy levels of the singlet and triplet excited states in the protonated and non-protonated ligand, in order to compare them to the energy level of the Eu^{3+} and assess how protonation might change the emission mechanism. The authors found that the non-protonated ligand triplet state was located 3500 cm^{-1} higher than the $^5\text{D}_0$ transition of Eu^{3+} , which is in the optimal range for energy transfer from the ligand to the metal. However, upon protonation, the energy of the ligand triplet state drops to just 900 cm^{-1} above the Eu^{3+} $^5\text{D}_0$ transition, allowing back-transfer from the Eu^{3+} to the ligand and quenching emission.

The fast and sensitive detection of HCl gas through the use of a copper (I) iodide-based MOF $\text{Cu}_4\text{I}_4\text{L}$ (**1**, $\text{L} = 5,5',5''$ -(2,4,6-triethylbenzene-1,3,5-triyl)tris(2-(pyridin-4-yl)-1,3,4-oxadiazole)) was recently reported by Dong et al.¹¹⁰ **1** was synthesized under ambient conditions through the combination of CuI and **L** in acetonitrile, and gave a structure with two crystallographically-distinct Cu_4I_4 clusters linked into a doubly interpenetrated 3D framework by the ligand **L**. Upon exposure to 200 ppm HCl, **1** changed color from orange to dark brown (figure 12). While PXRD identified no structural change, a starch assay identified molecular iodine present in the pores of the material, with Raman analysis, XPS, and ion chromatography confirming that exposure to the HCl gas induced an I^-/Cl^- ion exchange in the Cu_4I_4 core that liberated I^- . The I^- was then oxidized by atmospheric O_2 in the presence of H^+ to give I_2 , which in turn provided the colorimetric shift observed (figure 12). The colorimetric shift observed was extremely sensitive, with HCl concentrations of as little as 4 ppb causing a clear difference in color. Because of the ion-

exchange nature of the interaction, **1** is extremely selective for HCl gas, and no response was observed in the presence of other similar gaseous acids, such as HF, HBr, HI, HOAc, HNO_3 , and HClO_4 . To increase the practical applicability, a composite material of **1** embedded in a polymer matrix was prepared in a single-step, one-pot process. CuI and **L** were combined under ambient conditions in a DMF/acetonitrile solution containing the polymer binder polyvinylidene fluoride. Acetonitrile was then removed from the solution under vacuum, resulting in a homogenous suspension of micro-sized **1** and polymer binder in DMF, with the content of **1** being up to 69 wt%. The suspension was cast and dried at 90°C to give a mixed-membrane matrix (**1@MMM**). **1@MMM** was homogenous and maintained the porosity of **1**. When exposed to HCl vapor, **1@MMM** showed the same sensitivity with a visual detection limit of 3.2 ppb and a luminescent detection limit of 1.6 ppb; both are significantly lower than the 5 ppm workplace exposure limit. Additionally, because of the film's relative thinness and correspondingly increased contact area, the response of **1@MMM** is much faster, with full color change observable after 1 minute of exposure.

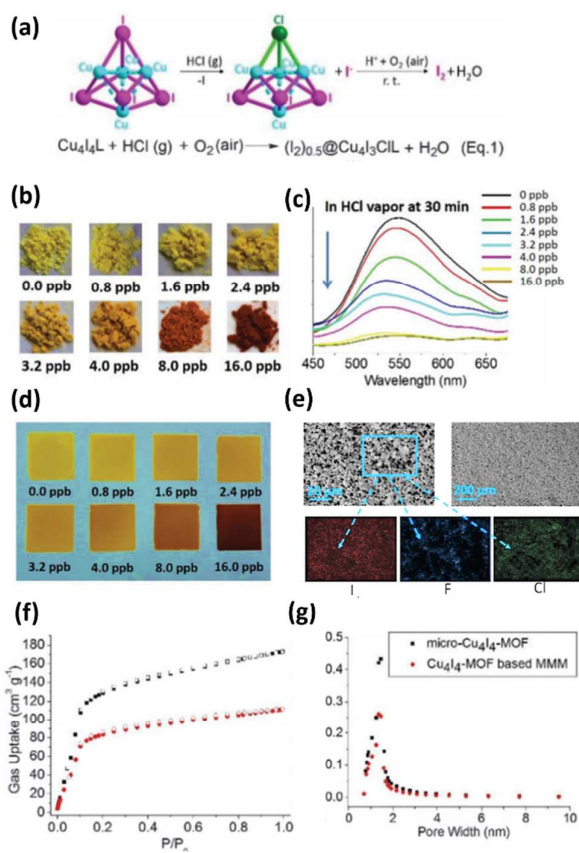


Figure 12. (a) Sensing mechanism of **1** upon exposure to HCl gas. (b) Samples of **1** exposed to various concentrations of HCl gas. (c) Emission from **1** under 370 nm excitation following exposure to various concentrations of HCl gas. (d) Samples of **1@MMM** following exposure to various concentrations of HCl gas. (e) SEM images of **1@MMM** following exposure to HCl gas at high (top left) and low (top right) magnification, with EDS mapping shown for I, F, and Cl. (f) CO_2 adsorption isotherms for **1** (black) and **1@MMM** (red). (g) Pore width distribution of **1** and **1@MMM**.¹¹⁰

Reproduced from ref. 110 with permission from the Royal Society of Chemistry, copyright 2016.

2.4 Detection of CWAs

Unlike the previously described chemical species, whose toxicity arises incidentally, chemical warfare agents (CWAs) have been designed to maximize the negative impact they can have on human health. The two main categories of modern CWAs are blistering agents, such as sulfur mustard or lewisite, and nerve agents, such as tabun, sarin, and VX. MOFs have been reported for detoxification of chemical warfare agents and liquid-phase absorbance and luminescent sensing, but vapor-phase detection has been lacking.¹¹¹⁻¹¹⁵ This is a concern, as these weaponized nerve agents are typically dispersed in the vapor-phase. Because of their acute toxicity, designing and testing sensor materials for nerve agents poses a practical challenge, so less toxic analogues are often used. Reports of LMOFs able to detect CWAs in the vapor phase are very limited at this time. However, those that have been reported are very recent, indicating that this important field may be beginning to grow.

A weakly-emissive 1D coordination polymer that is converted into a strongly luminescent 3D framework upon exposure to the thioethers dimethyl sulfide (DMS) and diethyl sulfide (DES)—an analogue for the blistering agent di-(2-chloroethyl) sulfide, or sulfur mustard—in the vapor phase was recently reported by Leznoff *et al.*¹¹⁶ The coordination polymer $\text{Cu}_{1/2}\text{Au}_{1/2}\text{CN}$ was initially chosen because of the strong affinity of Cu open metal sites for thioethers, and the author's previous work preparing the LMOFs $[\text{Cu}_{1/2}\text{Au}_{1/2}\text{CN}]_2(\text{DMS})$ and $[\text{Cu}_{1/2}\text{Au}_{1/2}\text{CN}]_2(\text{DES})$ in solution.¹¹⁷ However, the authors found that $\text{Cu}_{1/2}\text{Au}_{1/2}\text{CN}$ was unresponsive to DMS and DES vapors, as strong inter-chain Au-Au interactions enforced structural rigidity that prevented the necessary rearrangement imposed by the coordination of the analyte with the Cu (I) centers. The amount of Au (I) within the material was therefore reduced to give $\text{Cu}_{2/3}\text{Au}_{1/3}\text{CN}$, in order to limit the amount of direct Au-Au interactions. Upon exposure to DMS and DES vapors, emission from the material was strongly turned on (figure 13) and shifted from 380 nm under UV excitation to 460 nm (DMS) and 420 nm (DES) (figure 13). PXRD analysis confirmed that the material, following exposure to the thioether vapors, was isostructural with the previously reported $[\text{Cu}_{1/2}\text{Au}_{1/2}\text{CN}]_2(\text{DMS})$ and $[\text{Cu}_{1/2}\text{Au}_{1/2}\text{CN}]_2(\text{DES})$, confirming that the thioether sulfur was bonded to the Cu (I) atoms. The sample could be regenerated by either blowing thioether-free air over the sample for extended time, or by heating at 120 °C for 15 minutes. Following regeneration, thioether sensing could be repeated for multiple cycles (figure 13).

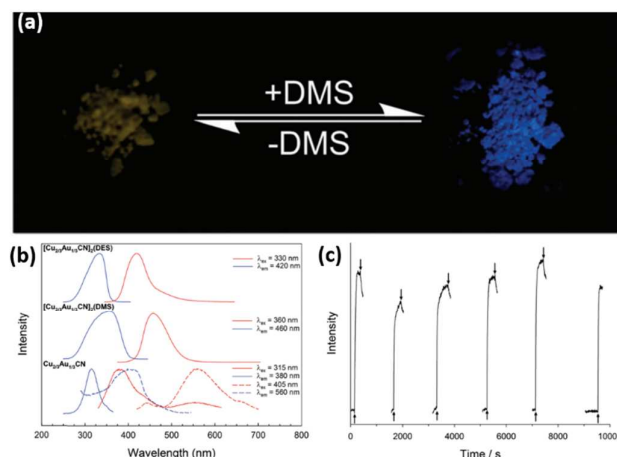


Figure 13. (a) $\text{Cu}_{2/3}\text{Au}_{1/3}\text{CN}$ before and after exposure to DMS vapor, with the response to DES vapor being visually identical. (b) Excitation and emission spectra of $\text{Cu}_{2/3}\text{Au}_{1/3}\text{CN}$ before and after exposure to DMS or DES. (c) Intensity of emission at 418 nm from $\text{Cu}_{2/3}\text{Au}_{1/3}\text{CN}$ over multiple cycles of exposure and regeneration, with regeneration achieved by heating the sample at 120 °C for 15 minutes.¹¹⁶ Reproduced from ref. 116 with permission from the Royal Society of Chemistry, copyright 2017.

The MOF HKUST-1 ($\text{Cu}_3(\text{btc})_2$, $\text{btc} = 1,3,5$ -benzenetricarboxylate) was recently reported to detect dimethyl chlorophosphate (DMCP), an analogue for G-series nerve agents including sarin and VX, in the vapor phase through a clear colorimetric shift.¹¹⁸ HKUST-1 was chosen for its open-copper sites, which the authors hoped with increase adsorption of the DMCP through coordination with the phosphate oxygen. HKUST-1 was mounted on a cotton textile (T-M) and exposed to DCMP vapor, resulting in a clear color change from turquoise to yellow (figure 14). Samples of HKUST-1 in combination with graphitic carbon nitride (MOFgCN) and oxidized graphitic carbon nitride (MOFgCNox) were also prepared and mounted on a cotton textile (T-MG and T-MGox, respectively). These composite materials not only showed colorimetric shifts when exposed to DCMP vapor, but T-MGox showed impressive DCMP absorbance of 670% wt% relative to Cu (I) and was also capable of degrading DCMP through visible light-driven hydrolysis.

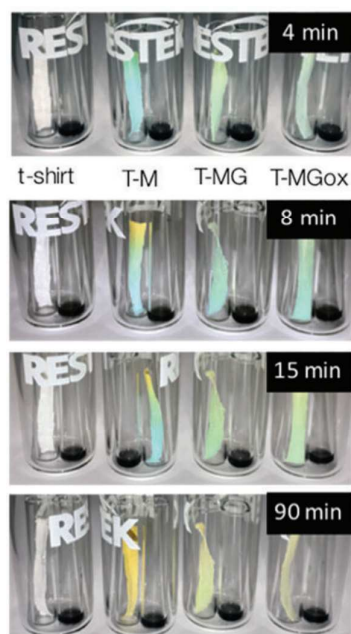


Figure 14. Color changes of cotton textile, T-M, T-MG, and T-MGox when exposed to DCMP vapors over time.¹¹⁸ Reproduced from ref. 118 with permission from the Royal Society of Chemistry, copyright 2017.

3. Adsorptive capture of toxic and hazardous gases and vapors by MOFs

In addition to effective detection capture and sequestration of toxic and hazardous species is also vital to prevent their potential threat on human health and/or the environment. Adsorptive capture represents a promising technology for the removal of toxic and hazardous gases and vapors as it is energy efficient and environmentally friendly. Various adsorbent materials have been proposed for this process.¹¹⁹⁻¹²¹ For example, carbon-based broad-spectrum filter is designed for removing toxic industrial gases. However, it suffers from low selectivity as amorphous carbons have broad pore size distribution.¹²² Additionally, carbon-based adsorbents usually have relatively weak affinity to polar adsorbates such as NH_3 or H_2S , resulting in low capacity.¹²² Thus, tailor-made adsorbent materials are needed for efficient removal of target species under specific conditions. The highly tunable nature of MOFs with respect to their composition, porosity, pore structure, and surface functionality renders them enormous advantages for adsorptive capture of toxic and hazardous gases. Though in some aspects the exploration is still in its early stage, MOFs have shown great potential and are promising for implementation in real-world systems.

Table 1. Selected FCs and CFCs with their boiling point and 100-year GWP (global warming potential)

Common name	Formula	Boiling point (°C)	100-year GWP (vs. CO_2)
CFC-11	CCl_3F	23.77	4660
CFC-12	CCl_2F_2	-29.8	10200

CFC-13	CCF_3	-81	13900
CFC-113	$\text{CCl}_2\text{FCClF}_2$	47.7	5820
CFC-114	$\text{CClF}_2\text{CClF}_2$	3.8	8590
CFC-115	CClF_2CF_3	-38	7670
HFC-23	CHF_3	-82.1	12400
HFC-32	CH_2F_2	-52	677
HFC-41	CHF_3	-78.4	116
HFC-125	CHF_2CF_3	-48.5	3170
HFC-134	CHF_2CHF_2	-23	1120
HFC-134a	CH_2FCF_3	-26.3	1300
HFC-143	CH_2FCHF_2	5	328
HFC-143a	CH_3CF_3	-47.6	4800
HFC-152	$\text{CH}_2\text{FCH}_2\text{F}$	31	16
HFC-152a	CH_3CHF_2	-25	138
HFC-161	$\text{CH}_3\text{CH}_2\text{F}$	-37.7	4
HFC-227ea	$\text{CF}_3\text{CH}_2\text{CF}_3$	-16.4	3350
HFC-236fa	$\text{CF}_3\text{CH}_2\text{CF}_3$	-1.4	8060
HFC-245fa	$\text{CHF}_2\text{CH}_2\text{CF}_3$	15.3	858
HCFC-22	CHClF_2	-40.8	1760
HCFC-123	CHCl_2CF_3	27.82	79
HCFC-124	CHFClCF_3	-12	527
HCFC-141b	CCl_2FCH_3	32	782
HCFC-142b	CClF_2CH_3	-9.2	1980
HCFC-225ca	$\text{CF}_3\text{CF}_2\text{CHCl}_2$	51	127
HCFC-225cb	$\text{CClF}_2\text{CF}_2\text{CHClF}$	56	525
PFC-14	CF_4	-127.8	6630
PFC-116	C_2F_6	-78.2	11100
PFC-218	C_3F_8	-36.7	8900
PFC-31-10	C_4F_{10}	-1.7	9200
PFC-41-12	C_5F_{12}	28	8,550
PFC-51-14	C_6F_{14}	56	7910
Halon-1211	CBrClF_2	-3.7	1750

3.1 Adsorption of fluorocarbons and chlorofluorocarbons

Fluorocarbons (FCs, including hydrofluorocarbons (HFCs)), and chlorofluorocarbons (CFCs, including hydrochlorofluorocarbons (HCFCs)) refer to hydrocarbon derivatives where one or more hydrogen atoms in hydrocarbons have been replaced by fluorine and/or chlorine atoms. They represent an important category of organic compounds that are ubiquitously involved in industry and our daily life. Their applications include use as solvents, refrigerants, and anesthetics, to name a few.^{39, 123} However, they have also given rise to tremendous safety and environmental concerns. Many FCs are greenhouses species with 100-year global warming potentials (GWPs, Table 1) 3-4 orders of magnitude higher than carbon dioxide, though they are present at a lower concentration in air.¹²⁴ CFCs, like the well-known Freon, are active ozone reducers which have destructive effects on the ozone layer. In light of their significant environmental impact, the use of CFCs has been heavily regulated since the late 1970s. For example, the United States banned the use of CFCs such as Freon in aerosol cans in 1978. In addition, a series of international treaties, including the well-known Montreal Protocol agreed to in 1987, have been ratified to protect the ozone layer by phasing out the production of substances that are responsible for ozone depletion. Since the beginning of the regulations against ozone depleting species, and especially since the adoption of the Montreal Protocol, the atmospheric concentration of many CFCs and related chlorinated hydrocarbons has noticeably

decreased. But despite the continued regulatory actions taken against the use of CFCs, they have never been completely phased out and still pose a threat to both the ozone layer and the climate. This is because the use of CFC-producing products has never been completely banned globally and related equipment is still in use, particularly in some developing countries. In addition, while the production and consumption of CFCs are regulated, emissions from products that already contain CFCs are unregulated. These products—refrigerators, air conditioners, and others—are a constant source of CFC emissions. More importantly, as the interim replacements for CFCs, HCFCs can also deplete the ozone layer, though to a lesser extent. In this context, the capture and sequestration of FCs and CFCs are imperative to expedite the complete elimination of ozone depleting species. FCs/CFCs adsorption related applications also include separation and/or enrichment of FCs/CFCs for recycling, FCs/CFCs-based adsorption heat pumps and so on.

Thallapally and co-workers¹²⁵ explored the adsorption of a series of fluorocarbon derivative refrigerants in selected MOFs including NiDOBDC, CoDOBDC, MIL-101-Cr, and MIL-100-Fe. MDOBDC (M = Ni and Co) features a microporous framework with a high density of open metal sites (OMSs) while MIL-101-Cr and MIL-100-Fe possess hierarchical pore structures with mesoporous cages connected through microporous windows. Thus the selected MOFs allow the effect of pore morphology and functionality on refrigerant adsorption to be investigated. The studied refrigerants include R-12 (CFC-12, CF_2Cl_2), R-13 (CFC-13, CClF_3), R-14 (PFC-14, CF_4), R-22 (HCFC-22, CHClF_2), and R-32 (HFC-32, CH_2F_2). All adsorbents show typical Type I adsorption profiles at room temperature (Figure 15). Adsorption of R-12 on NiDOBDC and CoDOBDC reaches saturation at relatively low pressure ($P/P_0 = 0.01$) with an uptake amount of 4.58 mol g^{-1} , which is more than twice the capacity of MIL-101-Cr ($< 2 \text{ mmol g}^{-1}$) at the same pressure. However, the saturation capacity of MIL-101 (at $P/P_0 = 0.6$) reaches 15 mmol g^{-1} , which is much higher than that of the other compounds. Grand Canonical Monte Carlo (GCMC) simulations suggest that at low pressure the primary adsorption site of R-12 is the OMSs for MDOBDC, while for MIL-101 it is preferentially adsorbed in the small pockets. By performing a column breakthrough measurement with a gas mixture of 90% He, 2% R-22 and 8% of R-12, the authors found MIL-101 can effectively separate the mixture into individual fractions. In light of the high adsorption capacity, especially at low pressure, and the separation ability toward FCs and CFCs, the authors concluded that these MOFs may be promising for FCs/CFCs adsorption/separation related applications.

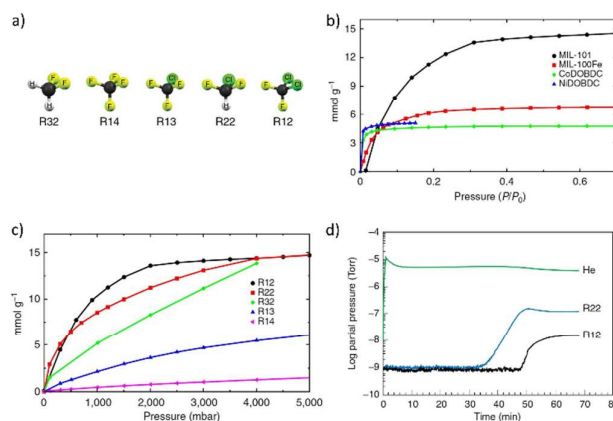


Figure 15. a) Molecular structure of FCs and CFCs. b) Adsorption isotherms of R-12 at 298 K in MDOBDC (M= Ni, Co), MIL-100-Fe, and MIL-101. c) Adsorption isotherms of various refrigerants in MIL-101 at 298 K. d) Experimental breakthrough of adsorption bed packed with MIL-101, a mixture of 90% He, 2% R-22, and 8% R-12 fed through the column with a flow rate of 0.25 ml min^{-1} .¹²⁵ Reproduced from ref. 125 with permission from the Nature Publishing Group, copyright 2014.

Miljanic and co-workers¹²⁶ reported the adsorption of FCs and CFCs by a noncovalent organic framework built on a highly fluorinated trispyrazole-based organic molecule (Figure 16a & 16b). The framework exhibits high thermal stability (stable up to $250 \text{ }^\circ\text{C}$), chemical stability (stable in common organic solvents, water, acidic and basic aqueous solutions) and high porosity (BET surface area: $1159 \text{ m}^2 \text{ g}^{-1}$). As expected, the material shows hydrophobic behavior with a contact angle of $132 \pm 1^\circ$ and it does not take up water even at 90% relative humidity, but exhibits favorable adsorption toward FCs and CFCs. It adsorbs 74 wt% of perfluorohexane at room temperature and no loss of capacity was observed after 20 adsorption/desorption cycles. In addition, the adsorption is very fast and reaches equilibrium in ~ 20 seconds. The compound shows similar adsorption behavior toward other FCs and CFCs including chloroform, dichloromethane, CFC-113 ($\text{CCl}_2\text{FCClF}_2$), and HCFC-225ca ($\text{CF}_3\text{CF}_2\text{CHCl}_2$). In a follow-up work,¹²⁷ the authors modify the organic molecule to a tritrazole ligand and subsequently incorporate it into a Cu-based metal-organic framework (MOFF-5, Figure 16c). It shows a BET surface area of $2445 \text{ m}^2 \text{ g}^{-1}$ with both micropores and mesopores. Adsorption of a number of FCs and CFCs was tested on MOFF-5, and high uptake capacity was observed for most of them due to its fluorinated structure and high porosity. MOFF-5 adsorbs as much as 225 wt% of perfluorohexane at room temperature, and the adsorption is complete within seconds of exposure (Figure 16d).

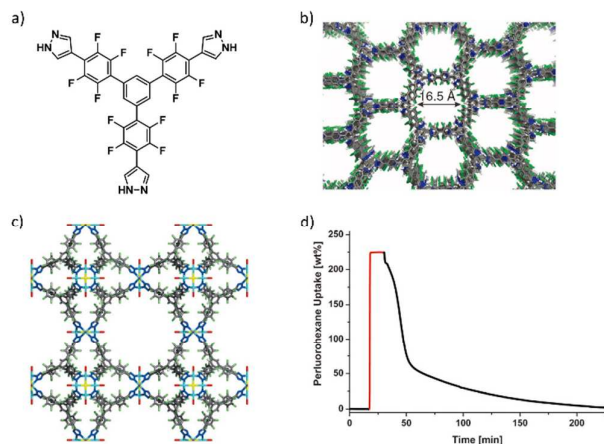


Figure 16. a) Molecular structure of the fluorinated monomer and b) crystal structure of the noncovalent organic framework. c) Crystal structure of MOFF-5 and d) its adsorption of perfluorohexane (C_6F_{14}) at room temperature. Black lines indicate the parts of the program when MOFF-5 was exposed only to N_2 stream, while red line describes the section of the program when N_2 carrying C_6F_{14} vapor was passed over MOFF-5.^{126,127} Reproduced from refs. 126 and 127 with permission from the Nature Publishing Group and the John Wiley & Sons, Inc, copyright 2014 and 2015, respectively.

Several MOF materials have been evaluated for the adsorption of R-22 ($HCFC-22$, $CHClF_2$). R-22 is a commonly used refrigerant. Due to its relatively low ozone depletion potential, R-22 was selected as an alternative to the highly ozone-depleting R-11 and R-12. However, the use of R-22 is no longer considered acceptable as a result of the enforcement of regulations against ozone depleting species. It has been mostly phased out in the United States and European Union, but its use in developing countries continues to increase owing to its high demand. Chen et al.¹²⁸ reported the adsorption of R-22 by a series of isorecticular MOFs with a formula of $Zn_4O(bpz)_2(ldc)$ ($bpz = 3,3',5,5'$ -tetramethyl-4,4'-bipyrazlate and $ldc =$ linear dicarboxylates including 1,4-benzenedicarboxylate, naphthalene-1,4-dicarboxylate, and biphenyl-4,4'-dicarboxylate). The porosity and pore size/shape of these compounds can be systematically tuned by changing the linear dicarboxylate linkers. R-22 adsorption isotherms were collected on these compounds at 273 and 313 K, and they all exhibit high adsorption capacity (80-120 wt% at 273 K and 1 bar, 65-75 wt% at 313 K and 1 bar). The high working capacity, relatively large adsorption enthalpies, and fast diffusion make these compounds promising candidates for R-22 capture and heat transformation systems.

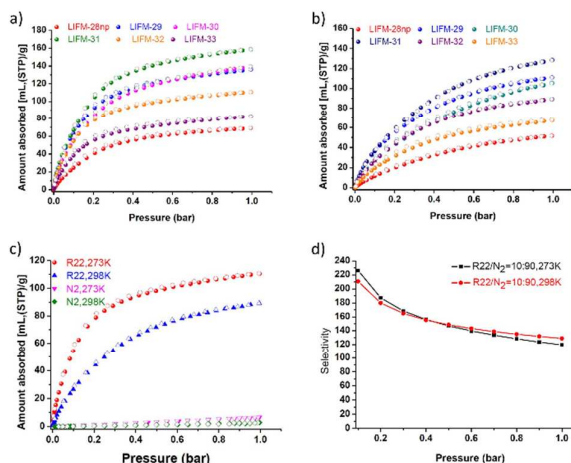


Figure 17. R-22 adsorption isotherms of LIFM-28np, LIFM-29, LIFM-30, LIFM-31, LIFM-32, and LIFM-33 at a) 273 K and b) 298 K. c) Adsorption isotherms of R-22 and N_2 on LIFM-32 at 273 K and 298 K. d) IAST selectivity of R-22/ N_2 on LIFM-32 at 273 K and 298 K.⁶⁵ Reproduced from ref. 65 with permission from the Royal Society of Chemistry, copyright 2017.

By a post-synthetic variable-spacer installation (SVSI) strategy, Su and co-workers¹²⁹ showed the fine-tuning of the porosity and pore surface of a series of Zr-MOFs modified from a prototype Zr-MOF, $Zr_6O_8(H_2O)_8(L^1)_4$ (LIFM-28, $L^1 = 2,2'$ -bis(trifluoromethyl)-4,4'-biphenyldicarboxylate). These materials have BET surface areas ranging from 940 to 1588 $m^2 g^{-1}$. Interestingly, it was found that the MOFs modified by ligand insertion show much higher adsorption capacity for R-22 (70-130 $cc g^{-1}$ at 298 K and 1 bar) and excellent R-22/ N_2 selectivity (170-290 calculated by IAST). In a follow-up work,⁶⁵ the authors applied the pore engineering strategy to PCN-700, an isostructural MOF of LIFM-28. By post-synthetic insertion of different dicarboxylate linkers, the authors were able to tune the pore environment and the adsorption performance of the materials. These compounds are highly porous, with BET surface areas of 1496-2222 $m^2 g^{-1}$, and they show both high adsorption capacity and selectivity toward R-22 (Figure 17). The R-22 uptake capacity and R-22/ N_2 IAST selectivity are 150-220 $cc g^{-1}$ (273 K and 1 bar) and 600-1000 (273 K and 1 bar, R-22/ $N_2 = 10:90$), respectively. These values are significantly higher than that of the pristine PCN-700. This was attributed to the pore space partition and pore surface modification by the inserted linkers.

Very recently, Motkuri and co-workers¹³⁰ reported the adsorption of another widely used refrigerant R-134a ($HFC-134a$, CH_2FCF_3) by Ni-MOF-74 and its derivative compounds. Through ligand modifications, the authors were able to engineer the pore structure and functionality of the MOFs. The saturated uptake capacities of R-134a are 0.58, 0.75, and 0.77 $g g^{-1}$ for Ni-MOF-74, Ni-MOF-74-BPP (BPP = 3,3'-dioxido-4,4'-biphenyldicarboxylate, biphenyl with para-COOH), and Ni-MOF-74-TPP (TPP = 3,3'-dioxido-4,4'-triphenyldicarboxylate, triphenyl with para-COOH), respectively, at 298 K while Ni-MOF-74 shows the highest adsorption enthalpy of 50.6 kJ/mol.

In situ FTIR analysis indicates the primary adsorption site for R-134a is the open Ni²⁺ centers.

3.2 Capture of radioactive gases and vapors

Among all energy sources which serve as alternatives to carbon-based fossil fuels, nuclear energy represents one of the most promising candidates in view of its low cost, high energy density, and low emission of greenhouse gases. Nuclear energy currently provides 11% of the world's electricity, and its contribution will undoubtedly continue to increase in light of the rapidly growing global energy demand.^{36, 131} However, in the process of mass implementation of nuclear power, we must safely capture and sequester the associated radioactive nuclear waste. While tremendous effort has been made to reprocess and recover heavy radioactive elements such as uranium and plutonium, less attention was paid to the volatile radioactive species, which include iodine, organic iodides, and krypton among others. These species are radiotoxic and highly volatile and must therefore be captured and removed from the off-gas mixtures to prevent their release into the environment.

In the process of nuclear waste management, off-gas streams containing volatile radioactive species (¹²⁹I₂, CH₃¹²⁹I, CH₃CH₂¹²⁹I, ¹⁴CO₂, ⁸⁵Kr etc.) as well as H₂O, nitric acid vapor, and NO_x are produced by dissolving used fuel rods in hot, concentrated (3–5 M) nitric acid. Thus, the proposed capture process involves selective adsorption of the target species from these off-gas mixtures.¹³² The capture usually relies on chemisorption or strong physisorption, as the interaction must be specific and selective for the targeted species in the presence of non-radioactive off-gas components. The current technology for I₂ removal involves the use of silver-exchanged zeolites which convert I₂ to AgI or AgIO₃.¹³³ However, these Ag-based sorbents have several disadvantages, including high cost, poor recyclability, and low capture capacity. In this context, various sorbent materials (silica, alumina, zeolites, activated carbons etc.) have been investigated for this application. A very recent example involves the use of all-silica zeolites for the capture of iodine and organic iodides.¹³² The authors found that hydrophobicity-intensified silicalite-1 (HISL), an exceptionally hydrophobic sorbent that is stable under highly acidic conditions, can effectively adsorb I₂, CH₃I, and CH₃CH₂I from a simulated acidic off-gas stream containing HNO₃ vapor and its decomposed products. At room temperature, its I₂ capture capacities under dry and simulated off-gas conditions are 53 wt% and 30 wt%, respectively. Similar capacities were observed for CH₃I and CH₃CH₂I. This compound outperforms many other sorbent materials under similar experimental conditions, and especially under simulated off-gas conditions. However, its disadvantages include relatively low adsorption capacity and poor capture capability at increased temperature. The former is limited by the low porosity of the sorbent, while the latter is attributed to the relatively weak adsorption affinity.

Metal-organic frameworks feature high porosity and exceptional tunability which render them enormous

advantages in addressing this challenge. Over the past few years, MOF materials have exhibited superior performance in the capture of volatile radioactive species.

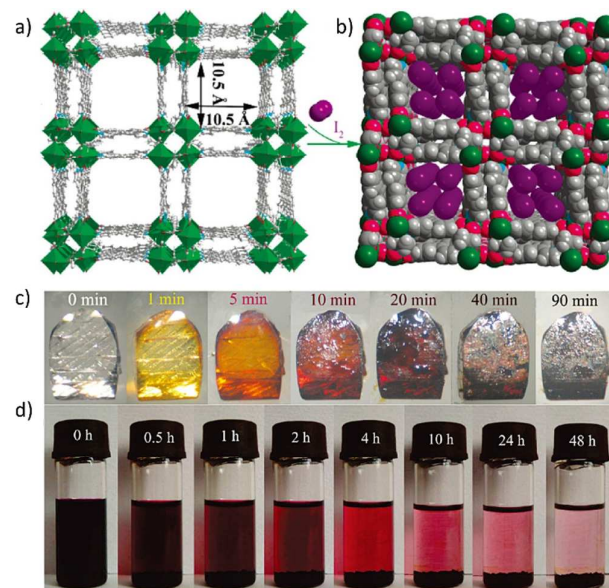


Figure 18. a) Crystal structure of Zn₃(DL-lac)₂(pybz)₂ showing the channels and b) sketch of I₂ molecules in the channels. c) Photographs showing the visual color change when a single crystal was immersed in the cyclohexane solution of I₂ (0.1 M/L). d) I₂ enrichment progress when 100 mg of crystals were soaked in 3 mL of a cyclohexane solution of I₂ (0.1 M/L).¹³⁴ Reproduced from ref. 134 with permission from the American Chemical Society, copyright 2010.

3.2.1. Iodine capture. Among all volatile radionuclides, iodine poses exceptional issues because of the particularly long half-life of ¹²⁹I (1.57 × 10⁷ years). In the early studies of I₂ adsorption by MOFs, I₂ was selected as a probe molecule to investigate the guest inclusion and removal behaviors. For example, Zeng and co-workers¹³⁴ reported a zinc-based rigid-pillared MOF, Zn₃(DL-lac)₂(pybz)₂ (DL-lac = DL-lactic acid, pybz = 4-(pyridine-4-yl)benzoic acid), and its controlled uptake and release of iodine. By suspending the desolvated MOF crystals in a cyclohexane solution of iodine, the authors observed a visual color change of the crystals from colorless through yellow and dark brown to black with time (Figure 18). The controllable release of iodine from the I₂-loaded MOF into organic solvent was also investigated. However, in these early explorations, the adsorption capacities were relatively low, since the sorbent materials were not designed for I₂ capture. Additionally, the I₂ loading experiments were performed at room temperature and commonly in solutions that are not actually relevant to nuclear waste management, which involves capture of I₂ vapor at relatively high temperature (75 °C). The first detailed study of iodine vapor capture was reported by Nenoff and coworkers.¹³⁵ In this study, ZIF-8 was selected for I₂ adsorption because of its large surface area (1810 m² g⁻¹), suitable pore aperture (3.4 Å), and high thermal and chemical stability.¹³⁶ The iodine loading was performed under typical fuel reprocessing conditions, ca. 350 K and ambient pressure. The maximum adsorption capacity of I₂ on

ZIF-8 was observed to be 125 wt% and was reached in several hours. This uptake amount was much higher than that of the traditional zeolite materials. It was observed that most of the adsorbed I_2 molecules were strongly trapped in the pores of ZIF-8 (Figure 19a); the weakly surface-adsorbed I_2 (25 wt%) were removed by heating the sample at 400 K for 1 hour, but no additional release of I_2 molecules was detected before the structure collapsed at 575 K. The synchrotron powder X-ray diffraction (PXRD) analysis revealed that the framework integrity was well maintained for I_2 loadings up to 70 wt% (1.3 I/Zn), beyond which the material lost its crystallinity. Following the loss of long-range order, however, the cage connectivity was actually retained, as indicated by PDF (pair distribution function) analysis. To evaluate the processability of ZIF-8 for I_2 capture from nuclear waste, the authors performed additional I_2 adsorption experiments on the extruded pellet form that is typically employed in real-world separation processes, and observed no change in I_2 adsorption performance compared to its powder form. In a follow-up study,¹³⁷ the authors found the retention of adsorbed I_2 molecules in ZIF-8 could be further improved by pressure-induced amorphization. Under a pressure of 0.34 GPa, the I_2 loaded ZIF-8 structure was amorphized, whereas the local cage structure with the captive I_2 remains intact. The mass losses corresponding to I_2 desorption shifted to higher temperatures by up to 150 °C for amorphized materials.

In this study, the iodine adsorption experiments were carried out at 75 °C with a 1:1 ratio of I_2 : H_2O vapor approximating the condition for real-world nuclear fuel reprocessing. During the adsorption process, the adsorbed amount was measured gravimetrically and confirmed by micro X-ray fluorescence. The maximum I_2 uptake was determined to be 175 wt%, corresponding to a loading of 3 I/Cu. This uptake capacity surpassed that of ZIF-8, the previous record holder. Unlike ZIF-8, which lost its long-range ordered structure upon high loading of I_2 , Cu-BTC retained its crystallinity at all I_2 loadings, as indicated by synchrotron-based XRD and PDF analysis. TGA-MS analysis of I_2 loaded Cu-BTC revealed no iodine or iodide species were released up to 150 °C, beyond which the evolution of iodide species was observed. I_2 adsorption sites in Cu-BTC were explored by a combination of MD (molecular dynamics) simulations and Rietveld analysis, which revealed two preferred adsorption positions (Figure 19b). One is in the smallest cage, and the other is located at the main pore. These adsorbed I_2 molecules interact with the axial water molecules coordinated to the paddle wheel metal centers via tritopic van der Waals interactions or with the benzene tricarboxylate organic linker. It is interesting to see that I_2 was preferentially adsorbed by hydrophilic Cu-BTC in the presence of moisture. The authors claim this is because the adsorbed I_2 molecules form a hydrophobic barrier preventing additional adsorption of water molecules.

While some MOF materials show exceptionally high iodine capture capacity, and molecular iodine can be temporarily trapped in their pores through strong I_2 -MOF interaction or by aforementioned pressure-induced amorphization, further conversion of I_2 loaded MOFs into long-term waste forms is imperative for safe sequestration of highly mobile iodine. In this context, Sava and co-workers¹⁴⁰ explored the use of glass-composite material (GCM) as long-term waste forms for I_2 loaded MOFs. Two different MOFs were selected for the study, ZIF-8 and HKUST-1, which were chosen for their low cost, high stability, and remarkable iodine capture capability. The authors first loaded iodine into the two MOFs through vapor adsorption at 75 °C (I_2 vapor pressure of 0.014 atm). 120 and 150 wt% of iodine was loaded for ZIF-8 and HKUST-1, respectively. The I_2 loaded MOFs were subsequently incorporated into low-sintering glass powder with the addition of silver flakes as an additional iodine scavenger. Glass-composite material (GCM) was formed at a sintering temperature of 500-525 °C. A typical GCM waste form was comprised of 80 wt% glass powder, 10 wt% I_2 loaded MOF, and 10 wt% silver flakes. The resulting GCMs exhibited exceptional thermal and chemical stability, and no release of iodine was detected during the sintering process or in the subsequent leach durability tests. Thus the incorporation of I_2 loaded MOFs into monolithic, highly robust GCM waste forms is an effective way for long-term sequestration of volatile iodine.

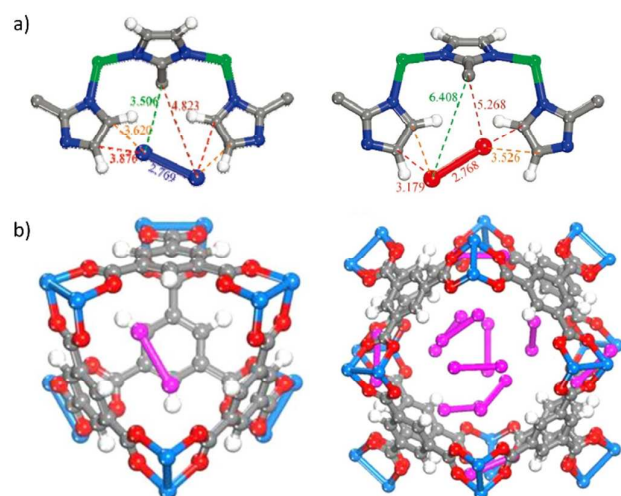


Figure 19. a) Two I_2 adsorption sites in the cage of ZIF-8. b) I_2 adsorbed in the small (left) and big (right) cage of HKUST-1.^{135,138} Reproduced from refs. 135 and 138 with permission from the American Chemical Society, copyright 2011 and 2013, respectively.

Cu-BTC (or HKUST-1, BTC= 1,3,5-benzenetricarboxylates) is another commercially available prototype MOF with high porosity.¹³⁹ Nenoff and co-workers¹³⁸ investigated I_2 capture by Cu-BTC and the competitive adsorption of water under humid conditions. Since the off-gas streams of nuclear waste are humid, it is crucial that the proposed sorbent materials retain their capture performance in the presence of moisture.

Table 2. Iodine adsorption by selected MOFs and porous organic materials

Adsorbent	BET surface area (m ² g ⁻¹)	Loading method	Temperature (°C)	I ₂ capacity (wt%)	Ref
UiO-66-PYDC	1030	I ₂ /cyclohexane solution	25	125	141
Zn ₃ (DL-lac) ₂ (pybz) ₂	763	I ₂ /hexane solution	25	101	134
TMU-16	-	I ₂ /hexane solution	25	45	142
Zn ₉ (btc) ₄ (atz) ₁₂	229	I ₂ /cyclohexane solution	25	40	143
Cu ₂ I ₂ (tppe)-1	303	I ₂ /cyclohexane solution	25	32	101
Cu ₂ I ₂ (tppe)-3	285	I ₂ /cyclohexane solution	25	30	101
JLU-Liu32	-	I ₂ /cyclohexane solution	25	29	144
Cd(2-NH ₂ bdc)(4-bpmh)	30	I ₂ /hexane solution	25	28	145
Cu ₂ I ₂ (tppe)-2	320	I ₂ /cyclohexane solution	25	27	101
JLU-Liu31	1700	I ₂ /cyclohexane solution	25	25	144
Cd(bdc)(4-bpmh)	36	I ₂ /hexane solution	25	14	145
Zn ₂ (tptc)(apy)(H ₂ O)	168	Iodine vapor	75	216	146
HKUST-1	1798	Iodine vapor (3.5 RH%)	75	175	138
ZIF-8	1810	Iodine vapor	75	125	135
Ni ₄ (44pba) ₈	-	Iodine vapor	25	110	147
MOC-19	-	Iodine vapor	25	50	148
Cu ₄ Cl ₃ (TPVS) ₄ (H ₂ O) ₂	-	Iodine vapor	70	49	149
(Cu) ₂ (tppe)	-	Iodine vapor	20	45	150
Fe ₃ (HCOO) ₆	385	Iodine vapor	25	35	151
Cd(L)(ClO ₄) ₂	-	Iodine vapor	25	32	152
Zn ₃ (BTC) ₂ (TIB) ₂	-	Iodine vapor	70	14	153
Cu ₄ I ₄ -MOF	641	Iodine vapor	25	13	154
Cd ₃ (BTC) ₂ (TIB) ₂	-	Iodine vapor	70	3	153
PAF-24	136	Iodine vapor	75	276	155
PAF-23	82	Iodine vapor	75	271	155
PAF-25	262	Iodine vapor	75	260	155
Azo-Trip	510	Iodine vapor	77	238	156
SCMP-2	855	Iodine vapor	77	222	157
CMP-E1	1213	Iodine vapor	75	215	158
CMPN-3	1368	Iodine vapor	70	208	159
NiP-CMP	2600	Iodine vapor	77	202	160
SCMP-1	413	Iodine vapor	77	188	157
PAF-1	5600	fixed pressure (40 Pa)	25	186	161
PAF-21	-	Iodine vapor	75	152	155
JUC-Z2	2081	fixed pressure (40 Pa)	25	144	161
CMPN-2	339	Iodine vapor	70	110	159
CMPN-1	230	Iodine vapor	70	97	159

Further improved I₂ capture capacity has been achieved by tailor-made materials. In a recent study, Zhang and co-workers¹⁴⁶ reported a record high I₂ uptake of 216 wt% by a NbO type MOF, Zn₂(tptc)(apy)(H₂O) (tptc⁴⁻ = terphenyl-3,3'',5,5''-tetracarboxylate, apy = aminopyridine). It has a BET surface area of 1470 m² g⁻¹, with aminopyridyl groups decorating the pore space. The authors attributed the exceptionally high I₂ adsorption capacity of this compound to its large porosity, plentiful phenyl rings, and strong electron-donor amino groups. Other than MOFs, some pure-organic based porous materials have also been designed for I₂ capture. Zhu and co-workers¹⁵⁵ designed and synthesized a series of charged porous aromatic frameworks (PAFs) by Sonogashira–Hagihara coupling reactions of lithium tetrakis(4-iodophenyl)borate and different alkyne monomers. These PAFs showed super high iodine adsorption capacity (> 250 wt% at 75 °C and ambient pressure), owing to multiple interactions between iodine and the charged aromatic frameworks with conjugated π-electrons. X-ray photoelectron spectroscopy (XPS) analysis revealed the encapsulated I₂ in the pores exist as

ionic I₃⁻, indicating the involvement of chemical reactions during iodine adsorption. Iodine adsorption performance in MOFs and other selected sorbents has been summarized in Table 2.

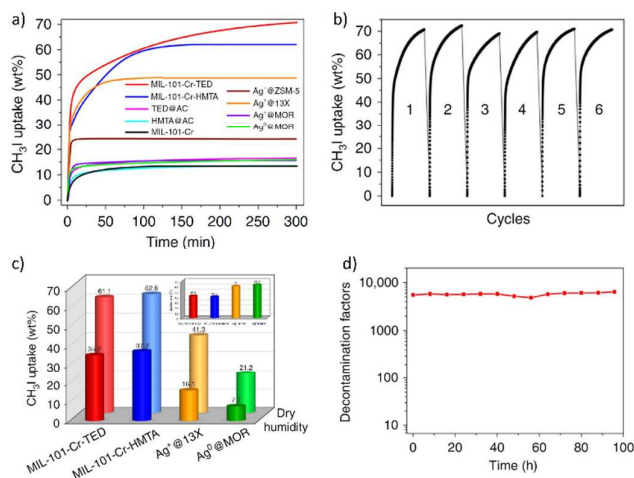


Figure 20. a) CH_3I adsorption curves in MIL-101-Cr-TED, MIL-101-Cr-HMTA, and selected benchmark sorbents at 150 °C with partial pressure of 0.2 atm. b) The recyclability of MIL-101-Cr-TED for CH_3I adsorption. Adsorption: 150 °C, 0.2 atm of CH_3I in nitrogen, desorption: removal of CH_3I together with TED and re-grafting TED; c) The CH_3I uptake at 150 °C under dry and humid (81%RH) conditions by breakthrough experiment. (back row: dry conditions; front row: humid conditions), (insert) the uptake drop ratio by comparing the CH_3I uptake of dry and humid conditions. d) Decontamination factors of CH_3I by MIL-101-Cr-TED under simulated conditions representing gas mixtures produced during CH_3I reprocessing, which include CH_3I (50 ppm), H_2O , HNO_3 , NO_2 , and NO at 150 °C.⁶⁷ Reproduced from ref. 67 with permission from the Nature Publishing Group, copyright 2017.

3.2.2. Capture of organic iodides. Radioactive organic iodides (ROIs) including CH_3I , $\text{CH}_3\text{CH}_2\text{I}$ etc. are another type of species commonly present in the off-gas streams of nuclear waste. Similar to the capture of iodine, current technology for the removal of radioactive organic iodides also involves the use of silver impregnated/exchanged solid sorbents such as silica, alumina, and zeolites.¹⁶²⁻¹⁶⁴ As mentioned earlier, this type of material suffers from high cost associated with the use of a noble metal and poor recyclability. Triethylenediamine (TED) impregnated activated carbon (AC) has also been proposed for this application.¹⁶² However, the capture of radioactive organic iodides is often performed at high temperature (e.g. 150 °C) in order to facilitate the desired chemical reactions and eliminate/diminish the impact from water adsorption. As AC-based materials are usable only under 120 °C, they are not suitable for these conditions. In addition, the presence of NO_x in the off-gas streams complicates the use of AC-based sorbents because of its low ignition temperature and the explosives that may form. Despite the fact that MOFs have been extensively explored for iodine capture as outlined above, their use for effectively trapping ROIs has not been exploited until the very recent work by our group. Inspired by the use of TED impregnated AC for the capture of ROIs, we designed a MOF-based molecular trap which exhibited exceptional ROI capture performance under both dry and simulated off-gas conditions (Figure 20)⁶⁷. The molecular trap was achieved by incorporating tertiary amines (TED and hexamethylenetetramine, HMTA) into a highly porous and robust MOF, MIL-101-Cr, via a coordination bond between N and the open Cr centers. The design rationale is that the tertiary

amine is grafted to the MOF framework by a single nitrogen atom, with the other end of the molecule (a N atom as well) decorating the pore surface and available as binding sites for organic iodides. The amine-functionalized materials, MIL-101-Cr-TED and MIL-101-Cr-HMTA, retained the same framework integrity as the original MOF and remained highly stable. The porosity of these two compounds showed a moderate decrease compared to the pristine structure, with BET surface areas of 2282 and 2272 $\text{m}^2 \text{g}^{-1}$ (vs 3342 $\text{m}^2 \text{g}^{-1}$ for MIL-101-Cr) for the TED and HMTA analogues, respectively. Despite this minor decrease, both are still much more porous than any other benchmark adsorbents which have surface areas of 300-1000 $\text{m}^2 \text{g}^{-1}$. The ROI uptake capacity for these tailor-made adsorbents was evaluated by vapor adsorption. At 30 °C, MIL-101-Cr-TED and MIL-101-Cr-HMTA adsorb 166 and 174 wt% of CH_3I respectively under a partial pressure of 0.2 atm. The adsorbed amounts are significantly higher than any other materials, which typically have uptakes of < 60 wt% under the same conditions. CH_3I adsorption experiments were also performed at 150 °C, which is more relevant to the capture of organic iodides from off-gas mixtures, and the CH_3I uptake amounts were 71 and 62 wt% for TED and HMTA impregnated MOFs, respectively. This also greatly outperformed other sorbent materials such as TED@AC, HMTA@AC, $\text{Ag}^+@ZSM-5$, and $\text{Ag}^+@MOR$. The exceptionally high CH_3I adsorption capacity of the tertiary amine functionalized MIL-101-Cr analogues was attributed to their high porosity and the effective grafting of TED and HMTA onto the pore surface, creating a molecular trap that greatly enhances the interaction with CH_3I . The adsorption performance for other organic iodides including $\text{CH}_3\text{CH}_2\text{I}$ and $\text{CH}_3\text{CH}_2\text{CH}_2\text{I}$ was also evaluated, and similar uptake capacities to CH_3I were observed. The authors further explored the material's capability of capturing ROIs under real-world conditions by performing column breakthrough experiments of a simulated off-gas mixture including CH_3I , I_2 , HNO_3 , and NO_x under high humidity (95% RH) at 150 °C. The total iodine uptake amounts are 38 and 33 wt% for MIL-101-Cr-TED and MIL-101-Cr-HMTA, respectively, which are more than twice higher than that of HISL (16 wt%) and $\text{Ag}^0@MOR$ (5 wt%) under the same conditions. These results demonstrate that the amine grafted MIL-101-Cr materials hold great promise for effective capture of iodine and organic iodides from off-gas streams. The ROI capture mechanism was investigated by various techniques including HRTEM-EDS, solid-state ^1H NMR, XPS, and *in situ* FT-IR, as well as theoretical calculations which support the proposed mechanism that the tertiary amines form strong chemical bonds with RI (R = $-\text{CH}_3$, $-\text{CH}_2\text{CH}_3$, or $-\text{CH}_2\text{CH}_2\text{CH}_3$) yielding ionic species (TED/HMTA-R)⁺ I⁻ at high temperatures. In a follow-up work,¹⁶⁵ we carried out a systematic study to investigate the effect of different amines on ROI capture. The selected amines included TED, HMTA, N,N-dimethylethylenediamine (DMEDA), N,N-dimethyl-1,3-propanediamine (DMPDA), and N,N-dimethyl-1,4-butanediamine (DMBDA). Adsorption results show that MIL-101-Cr-DMEDA gave the highest uptake amount (80 wt%) among the five amine functionalized compounds, which also represents a record-high value for all reported

sorbents. This can be attributed to its relatively high surface area ($2460 \text{ m}^2 \text{ g}^{-1}$) resulting from the smaller size of the functional amine (DMEDA). Remarkably, these amine functionalized MOF molecular traps can be recycled without loss of adsorption capacity.

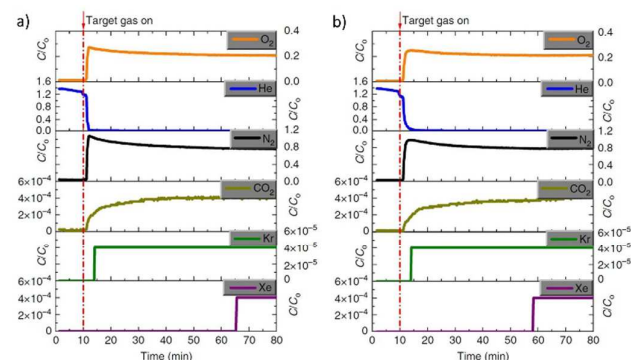


Figure 21. Column breakthrough experiments using CaSDB at room temperature and 1 atm. Inlet is a gas mixture with 400 ppm. Xe and 40 ppm. Kr balanced with air under a) dry and b) 42% relative humidity.¹⁶⁶ Reproduced from ref. 166 with permission from the Nature Publishing Group, copyright 2016.

3.2.3. Capture of noble gases. Other than radioactive iodine and organic iodides, the off-gas streams also contain noble gas radionuclides (predominately isotopes of Xe and Kr) which must be captured and sequestered.¹⁶⁶ ⁸⁵Kr is the larger concern because of its long half-life ($t_{1/2} = 10.8$ years).

The largest challenge to the adsorptive capture of noble gases is their inert nature. Traditional sorbents such as zeolites and activated carbons have been tested for noble gases capture and sequestration,³⁷ but they are generally plagued by low adsorption capacity owing to the inability to tune their pore geometry and functionality. MOFs hold great promise for the adsorption of noble gases because of their highly tunable structures and functionalities. To date, a variety of MOF materials have been studied for noble gases adsorption, and the progress in the field was recently reviewed.¹⁶⁷ Nevertheless, research has so far mostly been focused on the separation of Xe/Kr binary mixtures at relatively high partial pressure (> 0.1 bar), which is associated with Xe purification during air separation.^{166, 168, 169} In contrast, the capture of Xe or Kr from air (related to nuclear waste sequestration) has been rarely reported. In an early report, Liu and co-workers¹⁷⁰ investigated the capture capability of noble gases on HKUST-1 and NiDOBDC and found that NiDOBDC can adsorb and separate Xe/Kr from a simulated off-gas stream containing 400 p.p.m. Xe, 40 p.p.m. Kr, 78% N₂, 21% O₂, 0.9% Ar, and 0.03% CO₂. In a more recent study, Banerjee and co-workers¹⁶⁶ studied noble gases adsorption on a calcium based MOF, Ca(SDB) (SDB= sulfonyldibenzoate), which was identified as the most selective material for Xe/Kr adsorption out of a set of 125000 MOF structures through the use of a high-throughput computational screening method that modeled their performance. Experimental results confirm that Ca(SDB) shows the largest Henry coefficient of Xe adsorption ($38 \text{ mmol g}^{-1} \text{ bar}^{-1}$) and the highest Xe/Kr selectivity (derived from Henry

coefficients) among all reported materials. The high adsorption affinity toward noble gases on Ca(SDB) was attributed to its tailored pore size. Its Xe and Kr capture capability under dilute conditions was evaluated by column breakthrough experiments with a representative gas mixture (400 p.p.m. Xe, 40 p.p.m. Kr, 78.1% N₂, 20.9% O₂, 0.03% CO₂ and 0.9% Ar). The breakthrough curve shows that Kr and Xe are retained in the column for a longer time compared to other gas components. This is especially true of Xe, which exhibits a breakthrough time of more than 1 hour (Figure 21). The breakthrough experiment was also conducted under 42% relative humidity, and the adsorption capacity of Xe and Kr was mostly retained in the presence of water vapor.

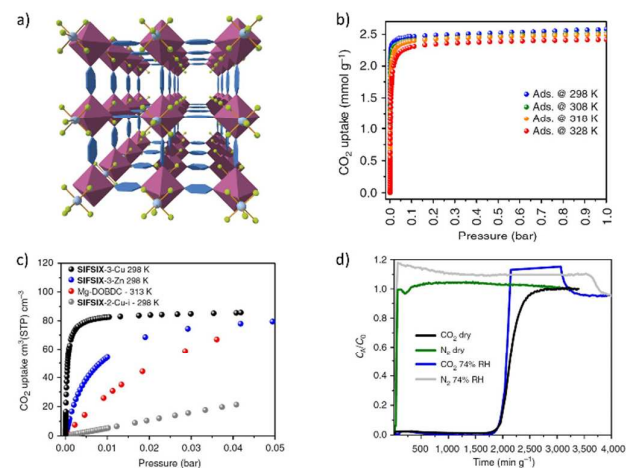


Figure 22. a) Crystal structure of SIFSIX-3-Cu. Color code: pyrazine: blue polygon, Cu: purple polyhedral, Si: light blue spheres, F: light green spheres. b) CO₂ adsorption isotherms at variable temperatures for SIFSIX-3-Cu. c) CO₂ volumetric uptake for SIFSIX-3-Cu at 298 K and low pressure, compared with SIFSIX-3-Zn, SIFSIX-2-Cu-I, and Mg-MOF-74. d) Column breakthrough test for CO₂/N₂: 1,000 p.p.m./99.9% for SIFSIX-3-Cu in dry as well as at 74% RH.¹⁷¹ Reproduced from ref. 171 with permission from the Nature Publishing Group, copyright 2014.

Table 3. Physical properties and toxicity data for selected industrial hazardous gases. 8-hour PEL represents 8-hour time-weighted average (TWA) permissible exposure limit set by Occupational Safety and Health Administration (OSHA).

Gas	Boiling point (K)	Kinetic diameter (Å)	8-hour PEL (ppm)
CO ₂	216.6	3.3	5000
CO	81.6	3.7	50
NH ₃	239.8	2.9	50
H ₂ S	212.8	3.6	20
NO ₂	294.3	4-5	5
NO	121	3.5	25
SO ₂	263	4.1	5

3.3 Capture of toxic industrial gases and chemical warfare agents

Toxic industrial gases (TIGs, Table 3) such as CO_x, NH₃, H₂S, SO_x, and NO_x are of particular concern because they are commonly involved in various industrial processes and are ubiquitous in the atmosphere. Removal of TIGs involves adsorption of target gases under varied situations. For example, as these toxic gases are used or produced in many

applications, industrial and emergency workers are at risk of exposure in the event of any accidental spills or leaks. Thus, efficient adsorbent materials for their capture are needed for protection or precaution. Additionally, certain toxic species are contained in flue gas or engine exhaust and must be removed before being released into the air. On the other hand, the direct capture of toxic gases from air is needed in areas where their concentration is above exposure limits. Compared to TIGs, CWAs are less common as a threat, since they are not as readily available as the former. However, due to their exceptionally high toxicity, capture and detoxification of CWAs is of utmost importance. CWAs are typically less volatile compared to other toxic and hazardous species; however, their vapors are still a serious threat as they are highly toxic. The removal of TIGs and CWAs by MOFs has become a burgeoning research area over the past few years, and related advancements have been reviewed recently from various perspectives.^{32, 33, 71, 172, 173} We will therefore focus on giving a general summary of material design strategies and highlighting significant progresses reported recently.

3.3.1 Capture of CO_x. Carbon dioxide (CO₂) has a IDLH (Immediately Dangerous to Life and Health) value of 40000 ppm, which is much higher than other hazardous gases such as NH₃ (300 ppm) and H₂S (100 ppm) and indicates its low toxicity. However, the environmental threat of CO₂ is not less than any other chemical, due to its implication in global warming as the primary greenhouse gas. Since CO₂ is predominantly emitted from the combustion of fossil fuels, implementation of CO₂ capture technologies to power plant flue gas could effectively lower the rising level of atmospheric CO₂. Adsorptive capture of CO₂ from flue gas by MOFs has been proposed as an alternative to the current capture technology involving the use of aqueous alkanolamine solutions, with the goal of at lowering the associated energy penalty. A more challenging application is direct air capture from the atmosphere. Although this is of prime importance, it is rarely addressed because of the low CO₂ partial pressures involved (< 420 ppm).^{174, 175} Tremendous effort has been made to develop MOFs for capturing CO₂ with high performance, and CO₂ adsorption is probably the most extensively explored application for MOFs. As a result, significant progress has been constantly reported, and MOF-based CO₂ capture technology holds promise for implementation in real-world systems. MOFs possessing open metal sites (OMSs) or with polar functional groups such as amines have shown preeminent CO₂ capture performance with respect to adsorption selectivity and capacity.³⁴ A prototype example is MOF-74 and its analogous/derivative materials. Long et al.^{81, 176} developed mmen-Mg₂(dobpdc) by amine grafting on the coordinatively unsaturated Mg²⁺ sites of Mg₂(dobpdc), an expanded MOF-74-Mg analogue. This material is able to adsorb 3.14 mmol g⁻¹ (12.1 wt%) of CO₂ at 0.15 bar and 40 °C, conditions associated with CO₂ capture from flue gas. Importantly, it is stable in the presence of water vapor and retains its affinity for CO₂ under humid conditions. Additionally, mmen-Mg₂(dobpdc) adsorbs 2.0 mmol g⁻¹ (8.1 wt%) of CO₂ at 25 °C at partial pressure as low as 0.39 mbar, suggesting its applicability for direct CO₂

capture from air. A mechanistic study revealed that the adsorption proceeds by cooperative insertion of CO₂ molecules into metal-amine bonds, leading to the formation of ammonium carbamate. Despite the chemisorption involved, the adsorbent is recyclable through temperature swings, with a regeneration energy appreciably lower than that of the aqueous amine solutions. In another work, through a crystal engineering or reticular chemistry strategy, Zaworotko, Eddaoudi and co-workers^{171, 177} developed a series of tailored microporous MOFs built on coordinatively saturated metal centers, periodically arrayed hexafluorosilicate (SiF₆²⁻) anions, and pyridyl ligands. In spite of the absence of OMSs or amine groups, these materials exhibit exceptional CO₂ capture performance even at very low pressure (Figure 22), attributed to their controllable pore size and favorable electrostatic interactions afforded by the SiF₆²⁻ anions. The heats of adsorption for CO₂ on these materials are lower than that of MOFs with OMSs, indicating a lower energy penalty associated with adsorbent regeneration. Remarkably, their CO₂ adsorption selectivity and capability is negligibly influenced by the presence of moisture. More recently, CO₂ capture by MOF-based membranes has attracted considerable research interest due to its high energy efficiency, low maintenance, and ease of processing. Significant advances have been made for developing both pure MOF membranes and mixed matrix membranes, as recently reviewed by Balbuena and co-workers.^{178, 179}

Carbon monoxide (CO) predominantly arises from the incomplete combustion of carbon-containing fuels. CO has a IDLH of 1200 ppm and threatens human health by causing tissue hypoxia. CO exposure is responsible for approximately 500 deaths annually. Research on CO adsorption by MOFs are mostly focused on those with OMSs such as MOF-74-M¹⁸⁰ (M= Zn²⁺, Ni²⁺, Co²⁺, Mg²⁺, Mn²⁺, Fe²⁺), HKUST-1,¹⁸¹ and MIL-101-Cr¹⁸² due to their favorable coordination to CO molecules. Long and co-workers⁸⁴ reported CO adsorption in a Fe-triazolate-based MOF, Fe-BTtri, with coordinatively unsaturated Fe²⁺ centers. It displays exceptional CO uptake capacity at low pressure (1.45 mmol g⁻¹ at 100 μbar and ambient temperature) and high adsorption selectivity over H₂, N₂, CO₂, and various hydrocarbons (Figure 23). The adsorption mechanism involves a spin state transition of the Fe²⁺ centers from high spin to low spin upon CO coordination. In a follow-up work,⁸⁵ the authors report two similar compounds where the iron (II) centers are linked into chains rather than the discrete nodes of the previous structure. The new structures, Fe₂Cl₂(bBTC) and Fe₂Cl₂(bTDD), adsorb CO through a cooperative spin transition mechanism. They exhibit a large CO working capacity with low regeneration energies and high selectivities over other gases which may enable the adsorbent for CO extraction from industrial waste feeds.

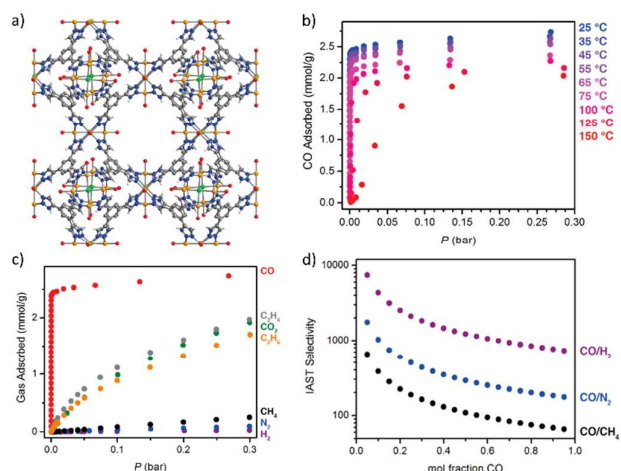


Figure 23. a) Crystal structure of Fe-BTtri. b) Carbon monoxide adsorption isotherms measured at various temperatures in Fe-BTtri. c) Adsorption isotherms of various gases collected at 25 °C for Fe-BTtri. d) IAST selectivities for CO/H₂, CO/N₂, and CO/CH₄ at varying concentrations at 25 °C and 1 bar of total pressure in Fe-BTtri.⁸⁴ Reproduced from ref. 84 with permission from the American Chemical Society, copyright 2016.

3.3.2 Capture of ammonia. Ammonia (NH₃) has an IDLH value of 300 ppm; exposure to high concentrations of ammonia may cause lung damage. The 15-minute and 8-hour exposure limits for ammonia are 35 and 25 ppm, respectively, set by OSHA (U.S. Occupational Safety and Health Administration). Ammonia is widely used as fertilizer, cleaner, and chemical feedstock, and it has a global production of 176 million tons in 2014. Ammonia spills are frequent, threatening industrial and emergency workers. MOFs have been investigated for ammonia capture because the currently employed carbon-based adsorbents generally suffer from low capacity. Various computational and experimental studies demonstrate that MOFs possessing OMSs or functional groups that form strong hydrogen bonds with ammonia display high adsorption capacity at low pressure. However, many of these materials undergo loss of crystallinity and porosity upon exposure to ammonia of relatively high concentration, due to exceptionally strong adsorbate-adsorbent interaction.⁹⁹ Dinca and co-workers¹⁰⁴ recently reported ammonia adsorption by a series of mesoporous MOFs, M₂Cl₂(BTDD)(H₂O)₂ (M= Mn, Co, and Ni), built on bisbenzene-triazolate ligands. Despite the presence of OMSs, these materials exhibit high and reversible ammonia uptake (Figure 24). They are able to adsorb 12.02–15.47 mmol g⁻¹ of ammonia at room temperature and 1 bar, and no loss of capacity was observed after three adsorption-desorption cycles. Although some MOFs have shown high ammonia adsorption capacities, competitive binding with water is a challenging issue which has not been well addressed. To this end, the use of hydrophobic MOFs may be a possible solution as demonstrated by computational studies. By GCMC simulations, Ghosh and co-workers¹⁰⁵ show that the NH₃ uptake capacities of hydrophobic MOFs do not suffer a dramatic drop in the presence of water. This is because ammonia molecules are in close contact with the pore surface

while water molecules are in the middle of the pores due to the hydrophobicity of the walls.

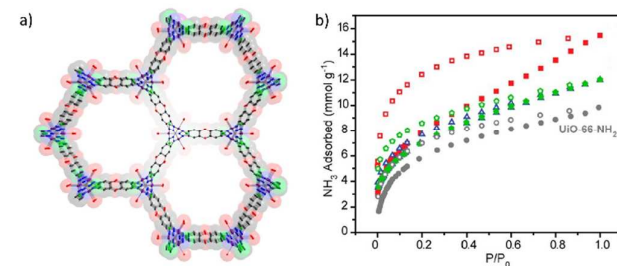


Figure 24. a) Crystal structure of M₂Cl₂(BTDD)(H₂O)₂ (M= Mn, Co, and Ni) b) NH₃ adsorption (solid symbols) and desorption (open symbols) for Mn (red squares), Co (blue triangles), and Ni (green pentagons) analogues, compared with UiO-66-NH₂ (grey circles).¹⁰⁴ Reproduced from ref. 104 with permission from the American Chemical Society, copyright 2016.

3.3.3 Capture of H₂S. Hydrogen sulfide (H₂S) is a highly toxic and corrosive gas with a characteristic smell of rotten eggs and an odor threshold of as low as 0.47 ppb. OSHA has set a 8-hour permissible exposure limit of 10 ppm for H₂S, above which it may cause eye irritation and damage. H₂S is mainly produced in oil refinement and natural gas production, and unacceptable amounts of H₂S must be removed from related gas streams. Various techniques have been applied to H₂S capture, including absorption in polar liquids and by porous solids such as carbons and zeolites.¹⁸³ MOFs have also been extensively explored for H₂S capture, and some of the MOFs studied have shown very high capacity. For example, MIL-101 can take up 38 mmol g⁻¹ of H₂S at 20 bar due to its large pore volume.¹⁸⁴ However, in real-world systems, H₂S capture involves the selective removal of the molecule from gas streams containing CO₂, CH₄ and other gases from ppm to percentage levels. Recently, Belmabkhout and co-workers¹⁸⁵ reported a fine-tuned Ga-soc-MOF for H₂S capture. The compound is built on Ga₃O(COO)₆ SBUs linked by abtc⁴⁻ (3,3',5,5'-zaobenzene tetracarboxylates) ligands. It has a BET surface area of 1350 m² g⁻¹ and shows a high H₂S tolerance and stability. The authors evaluated its H₂S removal capability by performing column breakthrough tests with a mixture of CO₂/H₂S/CH₄: 5/5/90 at room temperature. The results display a substantially longer retention time for H₂S (40 min g⁻¹) than that of CH₄ and CO₂ (less than 5 min g⁻¹), indicating the potential of this material for H₂S removal from refinery-off gases and natural gases.

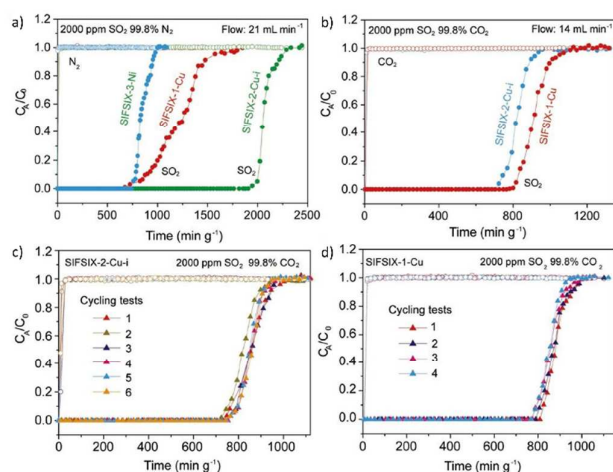


Figure 25. Experimental column breakthrough curves for a) SO_2/N_2 (2000 ppm SO_2) separations with SIFSIX-1-Cu, SIFSIX-2-Cu-i, and SIFSIX-3-Ni, and b) SO_2/CO_2 (2000 ppm SO_2) separations with SIFSIX-1-Cu and SIFSIX-2-Cu-i at 298 K and 1.01 bar. Cycling column breakthrough tests for CO_2/SO_2 (2000 ppm SO_2) separations with c) SIFSIX-2-Cu-i and d) SIFSIX-1-Cu at 298 K and 1.01 bar (mixed gas flow: 14 mL min^{-1}). In panel a), open circles are for N_2 , and filled circles are for SO_2 . In panels b-d), the open circles are for CO_2 , and the filled circles are for SO_2 . C_x/C_0 , outlet concentration/feed concentration.¹⁸⁶ Reproduced from ref. 186 with permission from the John Wiley & Sons, Inc, copyright 2017.

3.3.4 Capture of SO_2 and NO_2 . SO_2 and NO_2 are highly toxic acid gases that may damage the respiratory system upon exposure. Moreover, when dissolved in atmospheric water, they can both form acid rain. SO_2 and NO_2 are mainly emitted from automobiles and coal-fired power plants. MOF-based adsorptive capture technique has been proposed as an alternative to absorption by basic solutions for the removal of acidic gases, as the latter produces a large amount of wastewater. MOFs with OMSs such as MOF-74 and HKUST-1 are shown to have relatively high uptake amount and adsorption affinities toward NO_2 and SO_2 . Chabal and co-workers¹⁸⁷ investigated the interaction of NO_2 and SO_2 with MOF-74-M (M= Zn, Mg, Ni, Co) by *in situ* infrared spectroscopy and *ab initio* DFT calculations. While both gases interact strongly with OMSs, they exhibit distinct adsorption mechanisms. The bonding of NO_2 with metal centers leads to its dissociation, forming NO and NO_3^- . As for SO_2 , though it shows a high binding energy of 90 kJ mol^{-1} with the OMSs, the adsorption does not involve its chemical dissociation. NO_2 capture was also studied in stable Zr-based MOFs without OMSs, such as UiO-66 and UiO-67. Bandosz and co-workers¹⁸⁸ reported the influence of pore size on NO_2 adsorption. Under dry conditions, the smaller pore size of UiO-66 shows a positive impact on adsorption as a result of increased contact between the adsorbate and the pore walls. However, in the presence of moisture, the large pore size of UiO-67 enhances its adsorption of water, thus facilitating its uptake of NO_2 owing to the formation of nitric and nitrous acids in the pores. More recently, Peterson and co-workers¹⁸⁹ studied NO_2 removal from air (with NO_2 concentration of 500-700 ppm) by UiO-66- NH_2 under both dry and humid conditions. The functional amine group is found to considerably enhance NO_2

removal capability of the MOF. More importantly, NO_2 adsorption on UiO-66- NH_2 generates a substantially reduced amount of NO, compared to the activated carbon BPL which is the benchmark adsorbent for toxic gas filtration. Investigation of the adsorption mechanism revealed the formation of a diazonium ion on the aromatic ring of the MOF. Xing and co-workers¹⁸⁶ reported the use of inorganic anion (SiF_6^{2-}) pillared MOFs for SO_2 capture. They show exceptional SO_2 uptake capacity even at very low concentration (2.31 mmol g^{-1} at 0.002 bar, Figure 25), which was attributed to the strong electrostatic interaction between the SO_2 molecules and the anions/aromatic rings of the MOFs. Importantly, these materials exhibit highly favorable adsorption of SO_2 over CO_2 , which is not achievable by MOFs with OMSs such as MOF-74, yet is very important for SO_2 removal from flue gas due to the prevalence of CO_2 .

3.3.5 Capture of CWAs. Due to the extreme toxicity of chemical warfare agents (CWAs), their removal by MOFs have been typically done with simulant molecules. MOFs have been studied for not only the adsorptive capture but also the catalytic detoxification/degradation of CWAs, but this has been mostly performed in solution, which is out of the scope of this review.¹⁹⁰ Recently, Frenkel and co-workers⁶¹ reported the capture and decomposition of a nerve-agent simulant, dimethyl methyl phosphonate (DMMP) by a series of Zr-based MOFs including UiO-66, UiO-67, MOF-808, and NU-1000. The authors show that these MOFs are able to adsorb DMMP from air. EXAFS analysis indicates DMMP interacts directly with the Zr centers in the framework, leading to the hydroxylation of MOFs and the decomposition of DMMP. Thus, the integrity of the MOF structures is affected upon adsorption/desorption of DMMP to different degrees.

4. Conclusions and outlook

Over the past decade, researchers have shown that the physical and chemical properties of MOFs can be modified by various strategies, including substituting metal nodes/organic linkers, changing their connectivity, and post-synthetic functionalization, to name a few. The tremendous diversity and high tunability of MOFs allow the design of tailor-made materials with desirable features for specific applications. To this end, a considerable number of MOFs have been evaluated for their performance on sensing and/or capture of toxic and hazardous species. Some MOFs exhibit advantages over conventional materials in one or more aspects, however, some issues remain to be explored and addressed prior to their implementation in real-world applications.

Luminescence-based sensing has been a key area for LMOF research, and significant progress has been made in detecting nearly every class of compound.¹⁹ However, the great bulk of LMOF sensing has focused on analytes present in solution, rather than in the vapor or gas phase, despite the fact that many applications require detection to be done in the gas/vapor phase. Currently, the field of vapor and gas-phase sensing is under investigated. Even the subfields of vapor-phase sensing that have been explored, such as VOC sensing,

need more careful analysis. Often the reported work give the percentage by which emission can be quenched or enhanced, but fail to specify the analyte concentration associated with the emission change, or to investigate the detection limit. While MOF stability has improved from its early stage through the use of high valence metals or hydrophobic ligands, it is not uncommon for reports of new LMOF sensors to omit information on the stability of the sensor under real-world conditions. Furthermore, PXRD measurements are the most commonly cited evidence for the stability of a MOF under a given set of conditions. However, this only gives a broad picture of the sample's large-scale crystallinity, and fails to address issues such as altered pore or grain boundary conditions which can greatly affect sensing and gas adsorption applications. Surface area measurements, rather than PXRD, could provide a more nuanced view of MOF stability for applications that rely on mass transfer through that MOF, and its use as a stability assay should be more widely adopted. Additionally, improving sensing selectivity and decreasing response time remain challenging tasks for future development. Gas sensing by selective absorbance and pre-concentration of an analyte resulting in a luminescence change would be a powerful technique, but reports of such materials are very limited.⁵³ In many cases, this may be due to practical difficulties in combining gas adsorption and photoluminescence measurements.

With respect to the capture of hazardous gases and vapors, MOFs exhibit enormous potential for some specific applications, such as the capture of CO₂ from flue gas and radioactive molecular iodide and organic iodides from nuclear waste. However, for numerous other areas, current research remains at early stages, and therefore, considerable efforts are needed to address the existing challenges. First of all, while some MOFs show very high uptake capacity and/or adsorption selectivity toward certain molecule, the carefully designed linkers required complicated organic synthesis. The use of these exceptionally expensive ligands impedes their further consideration and evaluation for real applications. In addition, despite the fact that the stability of MOFs has improved markedly over the past several years, and some MOFs such as MIL-101-Cr and UiO-66 have shown exceptional thermal and chemical robustness that is comparable to inorganic adsorbents, a significant number of MOFs still suffer from relatively poor stability, particularly in regards to the loss of crystallinity and porosity upon prolonged exposure to water/acidic vapors at elevated temperature. Moreover, many of the adsorption experiments have been tested under conditions that are not relevant to industrial applications with respect to temperature, pressure, impurities, etc. While these measurements can provide some useful information regarding the adsorption capacity/selectivity of the adsorbent, further investigations under conditions comparable to the real world applications are necessary to fully evaluate the usefulness of the material.

Despite these challenges, research on metal-organic frameworks has been one of the fastest growing fields in material chemistry and will continue to advance in the future.

It offers incredible tunability for tailor-made material design and optimization, and true potential for applications in gas capture and sensing, as well as in many other areas.

Abbreviations

abtc	3,3',5,5'-zaobenzene tetracarboxylates
AC	activated carbon
apy	aminopyridine
atz	5-amino-tetrazole
Azo-Trip	azolinked microporous polymer
bbta	1H,5Hbenzo(1,2-d:4,5-d')bistriazole
BET	Brunauer–Emmett–Teller
bpdc	4,4'-biphenyldicarboxylate
bpe	1,2-bis(4-pyridyl)ethane
bpee	1,2-bipyridylethene
4-bpmh	N,N-bis-pyridin-4-ylmethylene-hydrazine
BPP	3,3'-dioxido-4,4'-biphenyldicarboxylate, biphenyl with <i>para</i> -COOH
bpy	4,4'-bipyridine
bpz	3,3',5,5'-tetramethyl-4,4'-bipyratole
BTC	1,3,5-benzenetricarboxylates
btdd	bis(1H-1,2,3-triazolo[4,5-b],[4',5'-i])dibenzo[1,4]dioxin
BTtri	1,3,5-tris(1H-1,2,3-triazol-5-yl)benzene
CFC	chlorofluorocarbon
CMP	conjugated microporous polymer
CMPN	conjugated microporous polymer nanotubes
CWA	chemical warfare agent
DL-lac	DL-lactic acid
DMBDA	N,N-dimethyl-1,4-butanediamine
DMEDA	N,N-dimethylethylenediamine
DMPDA	N,N-dimethyl-1,3-propanediamine
DMMP	dimethyl methyl phosphonate
DNT	dinitrotoluene
dobpdc	4,4'-dioxidobiphenyl-3,3'-dicarboxylate
DOBDC	2,5-dihydroxyterephthalate
FC	fluorocarbon
FRET	Fluorescence resonance energy transfer
GCM	glass-composite material
GCMC	Grand Canonical Monte Carlo
GWP	global warming potential
HCFC	hydrochlorofluorocarbons
HISL	hydrophobicity-intensified silicalite-1
HFC	hydrofluorocarbon
HMTA	Hexamethylenetetramine
IAST	ideal adsorbed solution theory
HMTA	hexamethylenetetramine
HOMO	highest occupied molecular orbital
L ¹	2,2'-bis(trifluoromethyl)-4,4'-biphenyldicarboxylate
L ²	2-hydroxymethyl-4,6-bis(2'-methoxy-4'-(2''-1''-carboxyl)-ethylene)-1,3,5-mesitylene
ldc	linear dicarboxylates
LC	ligand-centered

LLCT	ligand-to-ligand charge transfer
LMCT	Ligand-to-metal charge transfer
LMOF	luminescent metal-organic framework
LUMO	lowest unoccupied molecular orbital
1-mcp	1-methylcyclopropene
MLCT	metal-to-ligand charge transfer
MOF	Metal-organic framework
MOR	Mordenite
NAC	Nitroaromatic compounds
NB	nitrobenzene
ndc	2,6-naphthalenedicarboxylate
oba	4,4'-oxybis(benzoic acid)
OMS	open metal site
PAF	porous aromatic framework
44pba	4-(4-pyridyl)benzoate
pybz	4-(pyridine-4-yl)benzoate
PYDC	pyridine-dicarboxylic acid
RH	relative humidity
ROI	radioactive organic iodide
SBU	Secondary building unit
SCMP	Conjugated microporous polymers having thiophene building blocks
SDB	sulfonyldibenzoate
TED	triethylenediamine
TIB	1,3,5-tris(imidazol-1-ylmethyl)benzene
TPP	3,3'-dioxido-4,4'-triphenyldicarboxylate, triphenyl with <i>para</i> -COOH
tppe	1,1,2,2-tetrakis(4-(pyridin-4-yl)phenyl) ethane
tptc	terphenyl-3,3',5,5',-tetracarboxylate
TPVS	tetrakis(3-pyridyl)vinylsilane
VOC	Volatile organic compound

Acknowledgements

We would like to thank the US Department of Energy, Basic Energy Sciences, division of Materials Sciences and Engineering for support through Grant No. DE-FG02-08ER46491.

Notes and references

- S. R. Batten, N. R. Champness, X.-M. Chen, J. Garcia-Martinez, S. Kitagawa, L. Öhrström, M. O'Keeffe, M. Paik Suh and J. Reedijk, *Pure and Applied Chemistry*, 2013, 85, 1715-1724.
- O. K. Farha, I. Eryazici, N. C. Jeong, B. G. Hauser, C. E. Wilmer, A. A. Sarjeant, R. Q. Snurr, S. T. Nguyen, A. Ö. Yazaydin and J. T. Hupp, *J. Am. Chem. Soc.*, 2012, 134, 15016-15021.
- H. Furukawa, K. E. Cordova, M. O'Keeffe and O. M. Yaghi, *Science*, 2013, 341.
- Z.-F. Wu, B. Tan, M.-L. Feng, A.-J. Lan and X.-Y. Huang, *J. Mater. Chem. A*, 2014, 2, 6426.
- P. Silva, S. M. F. Vilela, J. P. C. Tome and F. A. Almeida Paz, *Chem. Soc. Rev.*, 2015, 44, 6774-6803.
- J. A. Mason, J. Oktawiec, M. K. Taylor, M. R. Hudson, J. Rodriguez, J. E. Bachman, M. I. Gonzalez, A. Cervellino, A. Guagliardi, C. M. Brown, P. L. Llewellyn, N. Masciocchi and J. R. Long, *Nature*, 2015, 527, 357.
- B. Li, H.-M. Wen, W. Zhou, Jeff Q. Xu and B. Chen, *Chem*, 2016, 1, 557-580.
- J. Sculley, D. Yuan and H.-C. Zhou, *Energy Environ. Sci.*, 2011, 4, 2721-2735.
- M. P. Suh, H. J. Park, T. K. Prasad and D.-W. Lim, *Chem. Rev.*, 2012, 112, 782-835.
- J.-R. Li, J. Sculley and H.-C. Zhou, *Chem. Rev.*, 2012, 112, 869-932.
- Z. Bao, G. Chang, H. Xing, R. Krishna, Q. Ren and B. Chen, *Energy Environ. Sci.*, 2016, 9, 3612-3641.
- H. Wu, Q. Gong, D. H. Olson and J. Li, *Chemical Reviews*, 2012, 112, 836-868.
- Z. R. Herm, E. D. Bloch and J. R. Long, *Chem. Mater*, 2014, 26, 323-338.
- X. Cui, K. Chen, H. Xing, Q. Yang, R. Krishna, Z. Bao, H. Wu, W. Zhou, X. Dong, Y. Han, B. Li, Q. Ren, M. J. Zaworotko and B. Chen, *Science*, 2016, 353, 141-144.
- L. Zhu, X.-Q. Liu, H.-L. Jiang and L.-B. Sun, *Chem. Rev.*, 2017, 117, 8129-8176.
- L. Zeng, X. Guo, C. He and C. Duan, *ACS Catal.*, 2016, 6, 7935-7947.
- Y.-B. Huang, J. Liang, X.-S. Wang and R. Cao, *Chem. Soc. Rev.*, 2017, 46, 126-157.
- L. Ma, J. M. Falkowski, C. Abney and W. Lin, *Nat. Chem*, 2010, 2, 838.
- W. P. Lustig, S. Mukherjee, N. D. Rudd, A. V. Desai, J. Li and S. K. Ghosh, *Chem. Soc. Rev.*, 2017, 46, 3242-3285.
- Z. Hu, B. J. Deibert and J. Li, *Chem. Soc. Rev.*, 2014, 43, 5815-5840.
- Z. Hu, W. P. Lustig, J. Zhang, C. Zheng, H. Wang, S. J. Teat, Q. Gong, N. D. Rudd and J. Li, *J. Am. Chem. Soc.*, 2015, 137, 16209-16215.
- M. D. Allendorf, C. A. Bauer, R. K. Bhakta and R. J. T. Houk, *Chem. Soc. Rev.*, 2009, 38, 1330-1352.
- A.-L. Li, Q. Gao, J. Xu and X.-H. Bu, *Coord. Chem. Rev.*, 2017, 344, 54-82.
- F.-M. Zhang, L.-Z. Dong, J.-S. Qin, W. Guan, J. Liu, S.-L. Li, M. Lu, Y.-Q. Lan, Z.-M. Su and H.-C. Zhou, *J. Am. Chem. Soc.*, 2017, 139, 6183-6189.
- G. K. H. Shimizu, J. M. Taylor and S. Kim, *Science*, 2013, 341, 354-355.
- P. Ramaswamy, N. E. Wong and G. K. H. Shimizu, *Chem Soc Rev*, 2014, 43, 5913-5932.
- Y. Zhao, *Chem. Mater*, 2016, 28, 8079-8081.
- C. Pettinari, F. Marchetti, N. Mosca, G. Tosi and A. Drozdov, *Polymer International*, 2017, 66, 731-744.
- A. Cadiau, K. Adil, P. M. Bhatt, Y. Belmabkhout and M. Eddaoudi, *Science*, 2016, 353, 137-140.
- Nat. Chem*, 2016, 8, 987.
- M. J. Clinton *N. Engl. J. Med.*, 1948, 238, 51-54.
- J. B. DeCoste and G. W. Peterson, *Chem. Rev.*, 2014, 114, 5695-5727.
- P. Kumar, K.-H. Kim, E. E. Kwon and J. E. Szulejko, *J. Mater. Chem. A*, 2016, 4, 345-361.
- K. Sumida, D. L. Rogow, J. A. Mason, T. M. McDonald, E. D. Bloch, Z. R. Herm, T.-H. Bae and J. R. Long, *Chem. Rev.*, 2012, 112, 724-781.
- R. Quadrelli and S. Peterson, *Energy Policy*, 2007, 35, 5938-5952.
- M. Lenzen, *Energy Convers. Manage.*, 2008, 49, 2178-2199.

37. N. R. Soelberg, T. G. Garn, M. R. Greenhalgh, J. D. Law, R. Jubin, D. M. Strachan and P. K. Thallapally, *Sci. Technol. Nucl. Install.*, 2013, 2013, 12.
38. L. Szinicz, *Toxicology*, 2005, 214, 167-181.
39. D. C. Wang, Y. H. Li, D. Li, Y. Z. Xia and J. P. Zhang, *Renewable Sustainable Energy Rev.*, 2010, 14, 344-353.
40. S. Srivastava, B. K. Gupta and R. Gupta, *Cryst. Growth Des.*, 2017, 17, 3907-3916.
41. L. Han, J. Zhou, X. Li, C.-Y. Sun, L. Zhao, Y.-T. Zhang, M. Zhu, X.-L. Wang and Z.-M. Su, *Inorg. Chem. Commun.*, 2017, 86, 200-203.
42. X.-Y. Xu and B. Yan, *Dalton Trans.*, 2016, 45, 7078-7084.
43. Z. Dou, J. Yu, H. Xu, Y. Cui, Y. Yang and G. Qian, *Micro. Meso. Mater.*, 2013, 179, 198-204.
44. J.-J. Liu, Y.-B. Shan, C.-R. Fan, M.-J. Lin, C.-C. Huang and W.-X. Dai, *Inorg. Chem.*, 2016, 55, 3680-3684.
45. X.-Y. Xu and B. Yan, *J. Mater. Chem. A*, 2017, 5, 2215-2223.
46. Z. Wei, Z.-Y. Gu, R. K. Arvapally, Y.-P. Chen, R. N. McDougald, J. F. Ivy, A. A. Yakovenko, D. Feng, M. A. Omary and H.-C. Zhou, *J. Am. Chem. Soc.*, 2014, 136, 8269-8276.
47. Z. Hu, G. Huang, W. P. Lustig, F. Wang, H. Wang, S. J. Teat, D. Banerjee, D. Zhang and J. Li, *Chem. Commun. (Cambridge, U. K.)*, 2015, 51, 3045-3048.
48. J. Heine and K. Mueller-Buschbaum, *Chem. Soc. Rev.*, 2013, 42, 9232-9242.
49. B. Zhao, N. Li, X. Wang, Z. Chang and X.-H. Bu, *ACS Appl. Mater. Interfaces*, 2017, 9, 2662-2668.
50. C. Zhang, L. Sun, Y. Yan, Y. Liu, Z. Liang, Y. Liu and J. Li, *J. Mater. Chem. C*, 2017, 5, 2084-2089.
51. W. P. Lustig, F. Wang, S. J. Teat, Z. Hu, Q. Gong and J. Li, *Inorg. Chem.*, 2016, 55, 7250-7256.
52. J. Zhang, W.-B. Yang, X.-Y. Wu, X.-F. Kuang and C.-Z. Lu, *Dalton Trans.*, 2015, 44, 13586-13591.
53. N. Yanai, K. Kitayama, Y. Hijikata, H. Sato, R. Matsuda, Y. Kubota, M. Takata, M. Mizuno, T. Uemura and S. Kitagawa, *Nat. Mater.*, 2011, 10, 787-793.
54. R.-W. Huang, Y.-S. Wei, X.-Y. Dong, X.-H. Wu, C.-X. Du, S.-Q. Zang and T. C. W. Mak, *Nat. Chem.*, 2017, 9, 689-697.
55. Y. Yu, J.-P. Ma, C.-W. Zhao, J. Yang, X.-M. Zhang, Q.-K. Liu and Y.-B. Dong, *Inorg. Chem.*, 2015, 54, 11590-11592.
56. J. Li, X. Yu, M. Xu, W. Liu, E. Sandraz, H. Lan, J. Wang and S. M. Cohen, *J. Am. Chem. Soc.*, 2017, 139, 611-614.
57. S. Chen, J. Zhang, T. Wu, P. Feng and X. Bu, *J. Am. Chem. Soc.*, 2009, 131, 16027-16029.
58. J. Tang and J. Wang, *RSC Adv.*, 2017, 7, 50829-50837.
59. C. Yang, J. Cheng, Y. Chen and Y. Hu, *Appl. Surf. Sci.*, 2017, 420, 252-259.
60. H. J. Park, J. K. Jang, S.-Y. Kim, J.-W. Ha, D. Moon, I.-N. Kang, Y.-S. Bae, S. Kim and D.-H. Hwang, *Inorg. Chem.*, 2017, 56, 12098-12101.
61. A. M. Plonka, Q. Wang, W. O. Gordon, A. Balboa, D. Troya, W. Guo, C. H. Sharp, S. D. Senanayake, J. R. Morris, C. L. Hill and A. I. Frenkel, *J. Am. Chem. Soc.*, 2017, 139, 599-602.
62. R. G. AbdulHalim, P. M. Bhatt, Y. Belmabkhout, A. Shkurenko, K. Adil, L. J. Barbour and M. Eddaoudi, *J. Am. Chem. Soc.*, 2017, 139, 10715-10722.
63. Z. Li, A. W. Peters, A. E. Platero-Prats, J. Liu, C.-W. Kung, H. Noh, M. R. DeStefano, N. M. Schweitzer, K. W. Chapman, J. T. Hupp and O. K. Farha, *J. Am. Chem. Soc.*, 2017, 139, 15251-15258.
64. A. H. Assen, Y. Belmabkhout, K. Adil, P. M. Bhatt, D.-X. Xue, H. Jiang and M. Eddaoudi, *Angew. Chem., Int. Ed.*, 2015, 54, 14353-14358.
65. C.-X. Chen, Q.-F. Qiu, C.-C. Cao, M. Pan, H.-P. Wang, J.-J. Jiang, Z.-W. Wei, K. Zhu, G. Li and C.-Y. Su, *Chem. Commun.*, 2017, 53, 11403-11406.
66. Y. G. Chung, D. A. Gómez-Gualdrón, P. Li, K. T. Leperi, P. Deria, H. Zhang, N. A. Vermeulen, J. F. Stoddart, F. You, J. T. Hupp, O. K. Farha and R. Q. Snurr, *Sci. Adv.*, 2016, 2.
67. B. Li, X. Dong, H. Wang, D. Ma, K. Tan, S. Jensen, B. J. Deibert, J. Butler, J. Cure, Z. Shi, T. Thonhauser, Y. J. Chabal, Y. Han and J. Li, *Nat. Commun.*, 2017, 8, 485.
68. S. M. Cohen, *Chem. Rev.*, 2012, 112, 970-1000.
69. D. Britt, D. Tranchemontagne and O. M. Yaghi, *Proc. Natl. Acad. Sci.*, 2008, 105, 11623-11627.
70. I. Spanopoulos, P. Xydias, C. D. Malliakas and P. N. Trikalitis, *Inorg. Chem.*, 2013, 52, 855-862.
71. N. S. Bobbitt, M. L. Mendonca, A. J. Howarth, T. Islamoglu, J. T. Hupp, O. K. Farha and R. Q. Snurr, *Chem. Soc. Rev.*, 2017, 46, 3357-3385.
72. A. C. Kizzie, A. G. Wong-Foy and A. J. Matzger, *Langmuir*, 2011, 27, 6368-6373.
73. C. Wang, X. Liu, N. Keser Demir, J. P. Chen and K. Li, *Chem. Soc. Rev.*, 2016, 45, 5107-5134.
74. M. Bosch, M. Zhang and H.-C. Zhou, *Adv. Chem*, 2014, 2014, 8.
75. Y. Bai, Y. Dou, L.-H. Xie, W. Rutledge, J.-R. Li and H.-C. Zhou, *Chem. Soc. Rev.*, 2016, 45, 2327-2367.
76. G. Férey, C. Mellot-Draznieks, C. Serre, F. Millange, J. Dutour, S. Surblé and I. Margiolaki, *Science*, 2005, 309, 2040-2042.
77. J. H. Cavka, S. Jakobsen, U. Olsbye, N. Guillou, C. Lamberti, S. Bordiga and K. P. Lillerud, *J. Am. Chem. Soc.*, 2008, 130, 13850-13851.
78. Y. Huang, W. Qin, Z. Li and Y. Li, *Dalton Trans.*, 2012, 41, 9283-9285.
79. K. Wang, H. Huang, W. Xue, D. Liu, X. Zhao, Y. Xiao, Z. Li, Q. Yang, L. Wang and C. Zhong, *Crystengcomm*, 2015, 17, 3586-3590.
80. Q. Sun, B. Aguila, G. Verma, X. Liu, Z. Dai, F. Deng, X. Meng, F.-S. Xiao and S. Ma, *Chem*, 1, 628-639.
81. T. M. McDonald, J. A. Mason, X. Kong, E. D. Bloch, D. Gygi, A. Dani, V. Crocellà, F. Giordanino, S. O. Odoh, W. S. Drisdell, B. Vlaisavljevich, A. L. Dzubak, R. Poloni, S. K. Schnell, N. Planas, K. Lee, T. Pascal, L. F. Wan, D. Prendergast, J. B. Neaton, B. Smit, J. B. Kortright, L. Gagliardi, S. Bordiga, J. A. Reimer and J. R. Long, *Nature*, 2015, 519, 303.
82. P. J. Landrigan, R. Fuller, N. J. R. Acosta, O. Adeyi, R. Arnold, N. Basu, A. B. Baldé, R. Bertolini, S. Bose-O'Reilly, J. I. Boufford, P. N. Breyse, T. Chiles, C. Mahidol, A. M. Coll-Seck, M. L. Cropper, J. Fobil, V. Fuster, M. Greenstone, A. Haines, D. Hanrahan, D. Hunter, M. Khare, A. Krupnick, B. Lanphear, B. Lohani, K. Martin, K. V. Mathiasen, M. A. McTeer, C. J. L. Murray, J. D. Ndahimananjara, F. Perera, J. Potočník, A. S. Preker, J. Ramesh, J. Rockström, C. Salinas, L. D.

- Samson, K. Sandilya, P. D. Sly, K. R. Smith, A. Steiner, R. B. Stewart, W. A. Suk, O. C. P. van Schayck, G. N. Yadama, K. Yumkella and M. Zhong, *The Lancet*, 2017.
83. 7 million premature deaths annually linked to air pollution. *World Health Organization news release*, 25 Mar 2014, <http://www.who.int/mediacentre/news/releases/2014/air-pollution/en/>, Accessed 11/09, 2017.
84. D. A. Reed, D. J. Xiao, M. I. Gonzalez, L. E. Darago, Z. R. Herm, F. Grandjean and J. R. Long, *J. Am. Chem. Soc.*, 2016, 138, 5594-5602.
85. D. A. Reed, B. K. Keitz, J. Oktawiec, J. A. Mason, T. Runčevski, D. J. Xiao, L. E. Darago, V. Crocellà, S. Bordiga and J. R. Long, *Nature*, 2017, 550, 96.
86. P. Kovacic and R. Somanathan, *J. Appl. Toxicol.*, 2014, 34, 810-824.
87. J. M. D. S. Roy Harrison, Frédéric Dor, and Rogene Henderson, *WHO Guidelines for Indoor Air Quality: Selected Pollutants*, World Health Organization, Geneva, 2010.
88. A. Lan, K. Li, H. Wu, D. H. Olson, T. J. Emge, W. Ki, M. Hong and J. Li, *Angew. Chem., Int. Ed.*, 2009, 48, 2334-2338.
89. A. Lan, K. Li, H. Wu, L. Kong, N. Nijem, D. H. Olson, T. J. Emge, Y. J. Chabal, D. C. Langreth, M. Hong and J. Li, *Inorg. Chem.*, 2009, 48, 7165-7173.
90. Z. Hu, S. Pramanik, K. Tan, C. Zheng, W. Liu, X. Zhang, Y. J. Chabal and J. Li, *Cryst. Growth Des.*, 2013, 13, 4204-4207.
91. J. Qin, B. Ma, X.-F. Liu, H.-L. Lu, X.-Y. Dong, S.-Q. Zang and H. Hou, *J. Mater. Chem. A*, 2015, 3, 12690-12697.
92. F. Wang, C. Dong, Z. Wang, Y. Cui, C. Wang, Y. Zhao and G. Li, *Eur. J. Inorg. Chem.*, 2014, 2014, 6239-6245.
93. S. Pramanik, C. Zheng, X. Zhang, T. J. Emge and J. Li, *J. Am. Chem. Soc.*, 2011, 133, 4153-4155.
94. D. Banerjee, Z. Hu and J. Li, *Dalton Trans.*, 2014, 43, 10668-10685.
95. D. Banerjee, Z. C. Hu, S. Pramanik, X. Zhang, H. Wang and J. Li, *Crystengcomm*, 2013, 15, 9745-9750.
96. S. Pramanik, Z. C. Hu, X. Zhang, C. Zheng, S. Kelly and J. Li, *Chem-Eur J*, 2013, 19, 15964-15971.
97. F.-Y. Yi, Y. Wang, J.-P. Li, D. Wu, Y.-Q. Lan and Z.-M. Sun, *Mater. Horiz.*, 2015, 2, 245-251.
98. A. H. Goldstein and I. E. Galbally, *Environ. Sci. Technol.*, 2007, 41, 1514-1521.
99. L. Huang, T. Badosz, K. L. Joshi, A. C. T. v. Duin and K. E. Gubbins, *J. Chem. Phys.*, 2013, 138, 034102.
100. H. Zhang, J. Yang, Y.-Y. Liu, S. Song and J.-F. Ma, *Cryst. Growth Des.*, 2016, 16, 3244-3255.
101. S.-S. Zhao, L. Chen, X. Zheng, L. Wang and Z. Xie, *Chem. - Asian J.*, 2017, 12, 615-620.
102. P. Mani, A. A. Ojha, V. S. Reddy and S. Mandal, *Inorg. Chem.*, 2017, 56, 6772-6775.
103. Y. Li, S. Zhang and D. Song, *Angew. Chem., Int. Ed.*, 2013, 52, 710-713.
104. A. J. Rieth, Y. Tulchinsky and M. Dincă, *Journal of the American Chemical Society*, 2016, 138, 9401-9404.
105. P. Ghosh, K. C. Kim and R. Q. Snurr, *J. Phys. Chem. C*, 2014, 118, 1102-1110.
106. Z. Bai, Y. Dong, Z. Wang and T. Zhu, *Environment International*, 2006, 32, 303-311.
107. G. Nickerl, I. Senkovska and S. Kaskel, *Chem. Commun. (Cambridge, U. K.)*, 2015, 51, 2280-2282.
108. J.-N. Hao and B. Yan, *Nanoscale*, 2016, 8, 2881-2886.
109. N. B. Shustova, A. F. Cozzolino, S. Reineke, M. Baldo and M. Dinca, *J. Am. Chem. Soc.*, 2013, 135, 13326-13329.
110. C.-W. Zhao, J.-P. Ma, Q.-K. Liu, X.-R. Wang, Y. Liu, J. Yang, J.-S. Yang and Y.-B. Dong, *Chem. Commun. (Cambridge, U. K.)*, 2016, 52, 5238-5241.
111. C. Montoro, F. Linares, E. Quartapelle Procopio, I. Senkovska, S. Kaskel, S. Galli, N. Masciocchi, E. Barea and J. A. R. Navarro, *J. Am. Chem. Soc.*, 2011, 133, 11888-11891.
112. M. J. Katz, J. E. Mondloch, R. K. Totten, J. K. Park, S. B. T. Nguyen, O. K. Farha and J. T. Hupp, *Angew. Chem., Int. Ed.*, 2014, 53, 497-501.
113. J. E. Mondloch, M. J. Katz, W. C. Isley, III, P. Ghosh, P. Liao, W. Bury, G. W. Wagner, M. G. Hall, J. B. De Coste, G. W. Peterson, R. Q. Snurr, C. J. Cramer, J. T. Hupp and O. K. Farha, *Nat. Mater.*, 2015, 14, 512-516.
114. S.-Y. Moon, A. J. Howarth, T. Wang, N. A. Vermeulen, J. T. Hupp and O. K. Farha, *Chem. Commun. (Cambridge, U. K.)*, 2016, 52, 3438-3441.
115. S.-R. Zheng, R.-L. Chen, Z.-M. Liu, X.-L. Wen, T. Xie, J. Fan and W.-G. Zhang, *CrystEngComm*, 2014, 16, 2898-2909.
116. B. R. Varju, J. S. Ovens and D. B. Leznoff, *Chem. Commun. (Cambridge, U. K.)*, 2017, 53, 6500-6503.
117. J. S. Ovens, P. R. Christensen and D. B. Leznoff, *Chem. - Eur. J.*, 2016, 22, 8234-8239.
118. D. A. Giannakoudakis, Y. Hu, M. Florent and T. J. Badosz, *Nanoscale Horiz.*, 2017, 2, 356-364.
119. W.-C. Li, H. Bai, J.-N. Hsu, S.-N. Li and C. Chen, *Ind. Eng. Chem. Res.*, 2008, 47, 1501-1505.
120. M. Ozekmekci, G. Salkic and M. F. Fella, *Fuel Processing Technology*, 2015, 139, 49-60.
121. J. Kazmierczak-Razna, P. Nowicki and R. Pietrzak, *Chem. Eng. Res. Des.*, 2016, 109, 346-353.
122. C. C. Rodrigues, D. de Moraes, S. W. da Nóbrega and M. G. Barboza, *Bioresour. Technol.*, 2007, 98, 886-891.
123. V. Ochoa-Herrera and R. Sierra-Alvarez, *Chemosphere*, 2008, 72, 1588-1593.
124. J. C. Laube, M. J. Newland, C. Hogan, C. A. M. Brennkmeijer, P. J. Fraser, P. Martinerie, D. E. Oram, C. E. Reeves, T. Röckmann, J. Schwander, E. Witrant and W. T. Sturges, *Nat. Geosci.*, 2014, 7, 266.
125. R. K. Motkuri, H. V. R. Annapureddy, M. Vijaykumar, H. T. Schaef, P. F. Martin, B. P. McGrail, L. X. Dang, R. Krishna and P. K. Thallapally, *Nat. Commun.*, 2014, 5, 4368.
126. T.-H. Chen, I. Popov, W. Kaveevitvachai, Y.-C. Chuang, Y.-S. Chen, O. Daugulis, A. J. Jacobson and O. Š. Miljanić, *Nat. Commun.*, 2014, 5, 5131.
127. T.-H. Chen, I. Popov, W. Kaveevitvachai, Y.-C. Chuang, Y.-S. Chen, A. J. Jacobson and O. Š. Miljanić, *Angewandte Chemie International Edition*, 2015, 54, 13902-13906.
128. R.-B. Lin, T.-Y. Li, H.-L. Zhou, C.-T. He, J.-P. Zhang and X.-M. Chen, *Chem. Sci.*, 2015, 6, 2516-2521.
129. C.-X. Chen, Z. Wei, J.-J. Jiang, Y.-Z. Fan, S.-P. Zheng, C.-C. Cao, Y.-H. Li, D. Fenske and C.-Y. Su, *Angew. Chem., Int. Ed.*, 2016, 55, 9932-9936.

130. J. Zheng, R. S. Vemuri, L. Estevez, P. K. Koech, T. Varga, D. M. Camaioni, T. A. Blake, B. P. McGrail and R. K. Motkuri, *J. Am. Chem. Soc.*, 2017, 139, 10601-10604.
131. S. Chu and A. Majumdar, *Nature*, 2012, 488, 294.
132. T. C. T. Pham, S. Docao, I. C. Hwang, M. K. Song, D. Y. Choi, D. Moon, P. Oleynikov and K. B. Yoon, *Energy Environ. Sci.*, 2016, 9, 1050-1062.
133. D. W. Colcleugh and E. A. Moelwyn-Hughes, *J. Am. Chem. Soc.*, 1964, 2542-2545.
134. M.-H. Zeng, Q.-X. Wang, Y.-X. Tan, S. Hu, H.-X. Zhao, L.-S. Long and M. Kurmoo, *J. Am. Chem. Soc.*, 2010, 132, 2561-2563.
135. D. F. Sava, M. A. Rodriguez, K. W. Chapman, P. J. Chupas, J. A. Greathouse, P. S. Crozier and T. M. Nenoff, *J. Am. Chem. Soc.*, 2011, 133, 12398-12401.
136. K. S. Park, Z. Ni, A. P. Côté, J. Y. Choi, R. Huang, F. J. Uribe-Romo, H. K. Chae, M. O'Keeffe and O. M. Yaghi, *Proc. Natl. Acad. Sci.*, 2006, 103, 10186-10191.
137. K. W. Chapman, D. F. Sava, G. J. Halder, P. J. Chupas and T. M. Nenoff, *J. Am. Chem. Soc.*, 2011, 133, 18583-18585.
138. D. F. Sava, K. W. Chapman, M. A. Rodriguez, J. A. Greathouse, P. S. Crozier, H. Zhao, P. J. Chupas and T. M. Nenoff, *Chem. Mater.*, 2013, 25, 2591-2596.
139. S. S.-Y. Chui, S. M.-F. Lo, J. P. H. Charmant, A. G. Orpen and I. D. Williams, *Science*, 1999, 283, 1148-1150.
140. D. F. Sava, T. J. Garino and T. M. Nenoff, *Ind. Eng. Chem. Res.*, 2012, 51, 614-620.
141. Z. Wang, Y. Huang, J. Yang, Y. Li, Q. Zhuang and J. Gu, *Dalton Trans.*, 2017, 46, 7412-7420.
142. V. Safarifar and A. Morsali, *CrystEngComm*, 2014, 16, 8660-8663.
143. Z.-Q. Jiang, F. Wang and J. Zhang, *Inorg. Chem.*, 2016, 55, 13035-13038.
144. S. Yao, X. Sun, B. Liu, R. Krishna, G. Li, Q. Huo and Y. Liu, *J. Mater. Chem. A*, 2016, 4, 15081-15087.
145. S. Parshamoni, S. Sanda, H. S. Jena and S. Konar, *Chem. - Asian J.*, 2015, 10, 653-660.
146. R.-X. Yao, X. Cui, X.-X. Jia, F.-Q. Zhang and X.-M. Zhang, *Inorg. Chem.*, 2016, 55, 9270-9275.
147. G. Mehlana, G. Ramon and S. A. Bourne, *Micro. Meso. Mater.*, 2016, 231, 21-30.
148. W.-Q. Xu, Y.-H. Li, H.-P. Wang, J.-J. Jiang, D. Fenske and C.-Y. Su, *Chem. - Asian J.*, 2016, 11, 216-220.
149. M. S. Deshmukh, A. Chaudhary, P. N. Zolotarev and R. Boomishankar, *Inorg. Chem.*, 2017, 56, 11762-11767.
150. H. Kitagawa, H. Ohtsu and M. Kawano, *Angew. Chem., Int. Ed.*, 2013, 52, 12395-12399.
151. Z. M. Wang, Y. J. Zhang, T. Liu, M. Kurmoo and S. Gao, *Adv. Funct. Mater.*, 2007, 17, 1523-1536.
152. Q.-K. Liu, J.-P. Ma and Y.-B. Dong, *Chem. Commun.*, 2011, 47, 7185-7187.
153. Y. Rachuri, K. K. Bisht, B. Parmar and E. Suresh, *J. Solid State Chem.*, 2015, 223, 23-31.
154. N.-X. Zhu, C.-W. Zhao, J.-C. Wang, Y.-A. Li and Y.-B. Dong, *Chem. Commun.*, 2016, 52, 12702-12705.
155. Z. Yan, Y. Yuan, Y. Tian, D. Zhang and G. Zhu, *Angew. Chem., Int. Ed.*, 2015, 54, 12733-12737.
156. Q.-Q. Dang, X.-M. Wang, Y.-F. Zhan and X.-M. Zhang, *Polymer. Chem.*, 2016, 7, 643-647.
157. X. Qian, Z.-Q. Zhu, H.-X. Sun, F. Ren, P. Mu, W. Liang, L. Chen and A. Li, *ACS Appl. Mater. Interfaces*, 2016, 8, 21063-21069.
158. E. Stockel, X. Wu, A. Trewin, C. D. Wood, R. Clowes, N. L. Campbell, J. T. A. Jones, Y. Z. Khimyak, D. J. Adams and A. I. Cooper, *Chem. Commun.*, 2009, 212-214.
159. Y. Chen, H. Sun, R. Yang, T. Wang, C. Pei, Z. Xiang, Z. Zhu, W. Liang, A. Li and W. Deng, *J. Mater. Chem. A*, 2015, 3, 87-91.
160. S. A. Y. Zhang, Z. Li, H. Xia, M. Xue, X. Liu and Y. Mu, *Chem. Commun.*, 2014, 50, 8495-8498.
161. C. Pei, T. Ben, S. Xu and S. Qiu, *J. Mater. Chem. A*, 2014, 2, 7179-7187.
162. C. M. González-García, J. F. González and S. Román, *Fuel Processing Technology*, 2011, 92, 247-252.
163. K. W. Chapman, P. J. Chupas and T. M. Nenoff, *J. Am. Chem. Soc.*, 2010, 132, 8897-8899.
164. K. Funabashi, T. Fukasawa and M. Kikuchi, *Nucl. Technol.*, 1995, 109, 366-372.
165. B. Li, X. Dong, H. Wang, D. Ma, K. Tan, Z. Shi, Y. J. Chabal, Y. Han and J. Li, *Faraday Discuss.*, 2017, 201, 47-61.
166. D. Banerjee, C. M. Simon, A. M. Plonka, R. K. Motkuri, J. Liu, X. Chen, B. Smit, J. B. Parise, M. Haranczyk and P. K. Thallapally, *Nat. Commun.*, 2016, 7, ncomms11831.
167. D. Banerjee, A. J. Cairns, J. Liu, R. K. Motkuri, S. K. Nune, C. A. Fernandez, R. Krishna, D. M. Strachan and P. K. Thallapally, *Acc. Chem. Res.*, 2015, 48, 211-219.
168. H. Wang, K. Yao, Z. Zhang, J. Jagiello, Q. Gong, Y. Han and J. Li, *Chemical Science*, 2014, 5, 620-624.
169. X. Chen, A. M. Plonka, D. Banerjee, R. Krishna, H. T. Schaef, S. Ghose, P. K. Thallapally and J. B. Parise, *Journal of the American Chemical Society*, 2015, 137, 7007-7010.
170. J. Liu, P. K. Thallapally and D. Strachan, *Langmuir*, 2012, 28, 11584-11589.
171. O. Shekhah, Y. Belmabkhout, Z. Chen, V. Guillerm, A. Cairns, K. Adil and M. Eddaoudi, *Nature communications*, 2014, 5.
172. E. Barea, C. Montoro and J. A. R. Navarro, *Chem Soc Rev*, 2014, 43, 5419-5430.
173. I. Ahmed and S. H. Jung, *J. Hazard. Mater.*, 2016, 301, 259-276.
174. J. G. Vitillo, *RSC Adv.*, 2015, 5, 36192-36239.
175. K. S. Lackner, *Science*, 2003, 300, 1677-1678.
176. T. M. McDonald, W. R. Lee, J. A. Mason, B. M. Wiers, C. S. Hong and J. R. Long, *J. Am. Chem. Soc.*, 2012, 134, 7056-7065.
177. P. Nugent, Y. Belmabkhout, S. D. Burd, A. J. Cairns, R. Luebke, K. Forrest, T. Pham, S. Ma, B. Space, L. Wojtas, M. Eddaoudi and M. J. Zaworotko, *Nature*, 2013, 495, 80-84.
178. J. Yu, L.-H. Xie, J.-R. Li, Y. Ma, J. M. Seminario and P. B. Balbuena, *Chem. Rev.*, 2017, 117, 9674-9754.
179. H. B. Tanh Jeazet, C. Staudt and C. Janiak, *Dalton Trans.*, 2012, 41, 14003-14027.
180. E. D. Bloch, M. R. Hudson, J. A. Mason, S. Chavan, V. Crocellà, J. D. Howe, K. Lee, A. L. Dzubak, W. L. Queen, J. M. Zadrozny, S. J. Geier, L.-C. Lin, L. Gagliardi, B. Smit, J. B. Neaton, S. Bordiga, C. M. Brown and J. R. Long, *J. Am. Chem. Soc.*, 2014, 136, 10752-10761.

181. Q. Min Wang, D. Shen, M. Bülow, M. Ling Lau, S. Deng, F. R. Fitch, N. O. Lemcoff and J. Semanscin, *Micro. Meso. Mater.*, 2002, 55, 217-230.
182. A. Aijaz, A. Karkamkar, Y. J. Choi, N. Tsumori, E. Rönnebro, T. Autrey, H. Shioyama and Q. Xu, *J. Am. Chem. Soc.*, 2012, 134, 13926-13929.
183. M. S. Shah, M. Tsapatsis and J. I. Siepmann, *Chem. Rev.*, 2017, 117, 9755-9803.
184. L. Hamon, C. Serre, T. Devic, T. Loiseau, F. Millange, G. Férey and G. D. Weireld, *J. Am. Chem. Soc.*, 2009, 131, 8775-8777.
185. Y. Belmabkhout, R. S. Pillai, D. Alezi, O. Shekhah, P. M. Bhatt, Z. Chen, K. Adil, S. Vaesen, G. De Weireld, M. Pang, M. Suetin, A. J. Cairns, V. Solovyeva, A. Shkurenko, O. El Tall, G. Maurin and M. Eddaoudi, *J. Mater. Chem. A*, 2017, 5, 3293-3303.
186. X. Cui, Q. Yang, L. Yang, R. Krishna, Z. Zhang, Z. Bao, H. Wu, Q. Ren, W. Zhou, B. Chen and H. Xing, *Adv. Mater.*, 2017, 29, 1606929-n/a.
187. K. Tan, S. Zuluaga, H. Wang, P. Canepa, K. Soliman, J. Cure, J. Li, T. Thonhauser and Y. J. Chabal, *Chem. Mater.*, 2017, 29, 4227-4235.
188. A. M. Ebrahim, B. Levasseur and T. J. Bandoz, *Langmuir*, 2013, 29, 168-174.
189. G. W. Peterson, J. J. Mahle, J. B. DeCoste, W. O. Gordon and J. A. Rossin, *Angew. Chem., Int. Ed.*, 2016, 55, 6235-6238.
190. J. E. Mondloch, M. J. Katz, W. C. Isley Iii, P. Ghosh, P. Liao, W. Bury, G. W. Wagner, M. G. Hall, J. B. DeCoste, G. W. Peterson, R. Q. Snurr, C. J. Cramer, J. T. Hupp and O. K. Farha, *Nat. Mater.*, 2015, 14, 512.

